Lymph Node Fibroblast Phenotypes and Immune Crosstalk Regulated by Podoplanin Activity

Spyridon Makris[1], Yukti Hari-Gupta[1], Jesús A. Cantoral-Rebordinos [1,2], Victor G. Martinez[1,3], Harry L. Horsnell[1], Agnesska C. Benjamin[1], Isabella Cinti[4], Martina Jovancheva[1], Daniel Shewring[1], Nicola Nguyen[1], Charlotte M. de Winde[1,5], Alice Denton[4], Sophie E. Acton[1*]

1. Stromal Immunology Group, MRC Laboratory for Molecular Cell Biology, University College London, Gower Street, London WC1E 6BT, UK.
2. Stem Cell and Human Development Laboratory, The Francis Crick Institute, 1 Midland Road, NW1 1AT.
3. Molecular Oncology Unit, Centro de Investigaciones Energéticas, Medioambientales y Tecnológicas (CIEMAT), Madrid, Spain.
4. *Department of Immunology and Inflammation, Imperial College London, London, W12 0NN, UK*
5. Department for Molecular Cell Biology and Immunology, Amsterdam UMC, location VUmc, De Boelelaan 1108, 1081 HZ Amsterdam, Netherlands.

* Lead Contact: Sophie E. Acton: s.acton@ucl.ac.uk

Key Words

Lymphoid Tissue

Fibroblast

Podoplanin

Inflammation

Stromal immunology

Abstract

Lymph nodes are uniquely organised niches for immune interactions. Fibroblastic reticular cells (FRCs) facilitate immune cell communication and regulate immune function by producing growth factors, chemokines and inflammatory cues. Stromal expression of the glycoprotein Podoplanin (PDPN) is required for lymph node development, but the requirement for PDPN signaling in FRCs in adult lymph nodes has not been directly tested. Using a conditional *in vivo* deletion model PDGFR$\alpha^{mGFP\Delta PDPN}$, scRNA-seq revealed that PDPN deletion increased inflammatory signalling in lymph nodes and disrupted stromal-immune cells crosstalk in steady state and during adaptive immune responses. We confirmed that PDPN/CLEC-2 signaling in FRCs switches transcriptional states and alters expression of immune related genes. We conclude that Podoplanin expression impacts the immunoregulatory properties of fibroblastic stroma in lymph nodes and is a key transcriptional regulator of fibroblast function in lymph nodes.

Summary: Podoplanin expression regulates the immunoregulatory properties of fibroblastic stroma in lymph nodes

42 **INTRODUCTION**

43

44 Lymph nodes are key organs for immunity, providing the ideal meeting points for immune cells and
45 coordinating the response to tissue damage and infection(*1–3*). Lymph nodes begin to develop at
46 E12.5-E13.5 and are initially composed of both haematopoietic lymphoid tissue inducer (LTi) and
47 stromal lymphoid tissue organiser cells (LTo) cells (*2*, *4*, *5*). The lymph node tissue supports the
48 recruitment of immune cells but can also support their expansion during inflammation(*1*, *6*, *7*).
49 Importantly, in order to accommodate rapidly rising cell numbers, lymph nodes need to reversibly
50 expand (*6*, *8*). Stromal cells constitute a small fraction (1-2%) of the total cells in the lymph node
51 however they are critical for supporting immune cells both during the steady state and disease. Much
52 is now known about the construction of lymphoid tissues through development, and the signals
53 required for commitment and differentiation of specialised lymphoid tissue stroma (*9–11*). However,
54 we do not know how mature, adult lymphoid tissues maintain immunoregulatory properties through
55 steady state and inflammatory contexts.

56

57 Fibroblastic reticular cells (FRCs) are the most abundant stromal cells of the lymph node forming an
58 interconnected network which supports both the structural integrity of lymph nodes (*12*) and the
59 various immune niches. Recent advances in scRNA-seq have shown high levels of heterogeneity of
60 FRCs and their ability to specifically support distinct niches of immune cells (*9*, *13*). FRCs express the
61 chemokines CCL19 and CCL21 to facilitate the meeting of antigen-presenting dendritic cells and naïve
62 T cells (*13–15*). FRCs proximal to high endothelial vessels express high levels ICAM-1 and VCAM-1,
63 important adhesion molecules, supporting the recruitment of both T and B lymphocytes from the
64 circulation (*16*). FRCs proximal to B cell follicles are characterised by their high expression of CCL21
65 and BAFF to support B cell survival (*17–19*). Fibroblastic reticular cells of lymph nodes are the
66 archetype 'immunofibroblast' with the power to coordinate adaptive immune responses. As lymph
67 nodes form in embryonic development, mesenchymal precursor cells expand and acquire specialized
68 immunological features to attract and retain immune cells. It is not understood how such a ubiquitous
69 cell type such as a fibroblast adapts to support immune functions.

70

71 A common feature of all FRC subsets in the lymph node is their expression of Podoplanin. Podoplanin
72 is a small transmembrane glycoprotein whose functions have been described in different contexts in
73 both health and disease and is important in platelet aggregation, the separation of the lymphatic and
74 endothelial vasculature, and in cell maturation and migration during development (*20*, *21*).
75 Podoplanin is expressed on several cell types including platelets, kidney podocytes (*22*), osteocytes

(*23*), alveolar epithelial cells (*24*), keratinocytes (*25*), lymphatic endothelial cells (LECs) (*2*, *26*, *27*) and constitutively expressed by FRCs (*28*). Moreover, Podoplanin levels are upregulated in inflamed tissues (*29*), rheumatoid arthritis (*30*), in cancer cells cancer-associated fibroblasts (*31*, *32*) and during infection (*33*). Podoplanin was first described as a ligand for dendritic cell (DC) migration through the interaction with C-type lectin CLEC-2 (*6*). Later it was shown that this same interaction promotes lymph node expansion through the regulation of FRC contractility and regulates the unilateral deposition of extracellular matrix into the conduit network (*5–7*, *34*). Podoplanin maintains actomyosin contractility via activation of the cytoskeletal regulators ezrin and moesin (*35*), two members of the ERM (ezrin, radixin and moesin) family, which tether the cortical actin cytoskeleton to integral proteins in the plasma membrane (*36*). Most recently, we have described Podoplanin as a mechanical sensor in FRCs required to trigger FRC proliferation in response to increasing tissue tension through lymph node expansion (*8*). Mice with full knockout of Podoplanin fail to develop lymph nodes (*37*) and die shortly after birth due to circulatory defects (*38*, *39*), therefore the function of Podoplanin has not been fully explored specifically in FRCs, or in adult lymphoid tissues. Our recent work suggests a more extensive role for Podoplanin in lymph node tissue function, beyond control of actomyosin contractility. We therefore undertook a detailed analysis of how the PDPN/CLEC-2 signalling axis determines transcriptional states in FRCs and directly test the role of Podoplanin in determining the immunoregulatory phenotypes of FRC subsets.

We utilised a mouse model (PDGFRα-mGFP-CreERT2) for conditional genetic manipulation of fibroblasts. Platelet derived growth factor alpha (PDGFRα) was chosen for its broad expression in mesenchymal cells and their progenitors. Further, PDGFRα has been identified as a universal fibroblast marker through extensive single cell transcriptomic analysis of fibroblasts across a range on tissues and inflammatory states (*9*). This model allows us to visualise the fibroblastic reticular network structure and to conditionally delete Podoplanin. In this way we can now assess the function of Podoplanin specifically in fibroblastic stroma of adult lymphoid tissues.

102 **RESULTS**

103 **Podoplanin deletion *in vivo* alters the transcriptional state of FRCs**

104 We generated a PDGFR$\alpha^{mGFP\Delta PDPN}$ mouse model to examine the function of Podoplanin on lymph node
105 fibroblasts and lymph node tissue function. This model targets fibroblastic stroma specifically, PDPN$^+$
106 lymphatic endothelial cells (LECs) are not labelled with GFP (Fig. 1A). Tamoxifen treatment of
107 PDGFR$\alpha^{mGFP\Delta PDPN}$ (ΔPDPN) reduced expression of Podoplanin by >50% in >48.9% of GFP$^+$ cells (lymph
108 node fibroblasts) (Fig. 1B)**.**

109

110 CD45$^-$CD31$^-$ cells (fibroblasts) were enriched from PDGFRa^{mGFP} (Control) and PDGFR$\alpha^{mGFP\Delta PDPN}$ (ΔPDPN)
111 lymph nodes 10 days post tamoxifen induction of Cre recombinase (fig. S1A). Cluster analysis
112 identified 12 populations of cells which mapped closely to the subpopulations identified by Rodda et
113 al. (*13*) (Fig. 1,C and D, table S1 to table S3, fig. S1B and fig. S2,A and B). We observed reduced *Pdpn*
114 expression in each of the *Pdgfra*$^+$ clusters, whereas the *Pdgfrb*$^+$ clusters were either *Pdpn* negative or
115 *Pdpn* levels were unaffected by the genetic deletion as expected (fig S2,C and D). In addition, we
116 describe a separate proliferative population of *Mki67*^{hi} FRCs and 2 different populations of double
117 negative cells (DNC) (Fig. 1,C and D, fig. S2B, and tables S1 to S3). The DNC were first described by
118 Malhotra et al. as a contractile pericyte population (*40*), and in concordance with their study we
119 confirm that they express *Acta2* (fig. S1B), *Ednra, Ednrb, Myl9* (fig. S2A), and are a distinct cell type
120 from FRCs since they are *Pdgfrb*$^+$ and *Pdgfra*$^-$ (Fig. 1,C and D and fig. S1C).

121

122 Using these data, we next compared the Control and ΔPDPN stromal populations using density plots
123 (stat_density_2d) (Fig. 1E). To quantify changes to subsets density, we performed neighbourhood
124 analysis using MiloR (*41*) (Fig. 1F). DNC subsets were unaffected which was expected since they do not
125 express *Pdgfra* and therefore are not targeted in our model. However, it is important to note that
126 ΔPDPN FRCs are transcriptionally distinct from these DNC. We observed reduced numbers of FRCs in
127 the *Ccl19*^{lo}, *Cxcl9*$^+$, and *Cd34*$^+$ subsets (blue neighbourhoods) (Fig. 1,D to F). ΔPDPN FRCs clustered
128 more densely in the *Nr4a1* and *Ccl19hi* regions (red neighbourhoods) (Fig. 1,E and F). We performed
129 trajectory analysis (Monocle 3) of the Control and ΔPDPN fibroblasts using progenitor markers CD34
130 and Pi16 as the initial trajectory point (fig. S2E, white circle). CD34 is a common precursor marker
131 associated with tissue maintenance across multiple organs and Pi16 expression has been described as
132 a marker for mesenchymal precursor cells (*9*, *42–44*). The trajectory data shows that the fibroblasts,
133 and especially the *Ccl21*$^+$ TRC population, lose specificity after deletion of Podoplanin (fig. S2E).
134 Overall, our data show that *Pdpn* expression significantly alters FRC phenotypes across the broad
135 range of subsets as defined by the field.

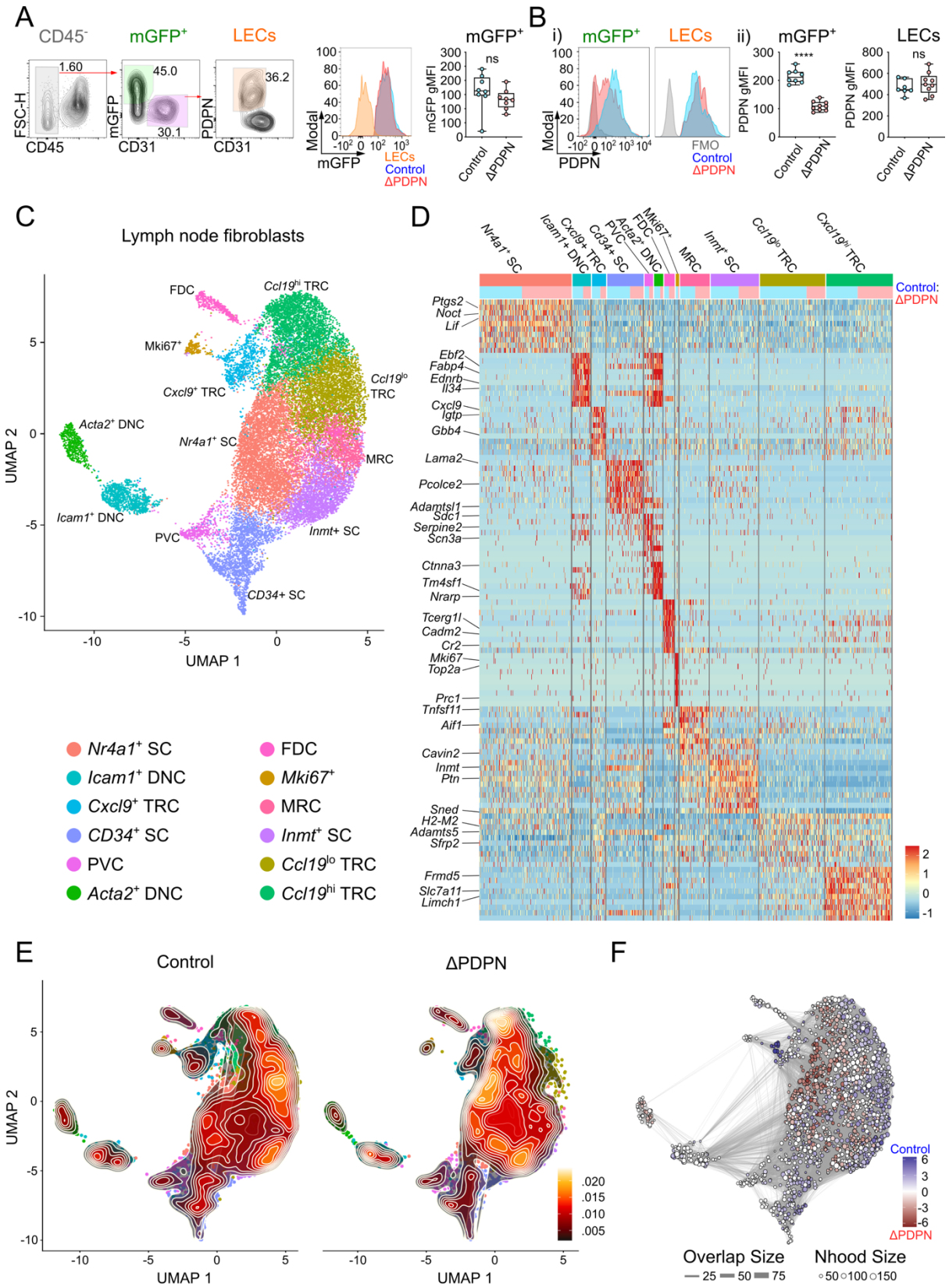

Fig. 1. Transcriptional state of fibroblasts is altered by podoplanin deletion.

(**A**) Flow cytometry gating of CD45⁻, mGFP⁺ (PDGFRα^{mGFP}) and lymphatic endothelial cells (LECs) with representative histograms of the mGFP expression for PDGFRα^{mGFP} (control) or PDGFRα$^{mGFP\Delta PDPN}$ (ΔPDPN) stroma with geometric mean fluorescence intensity (gMFI) for mGFP⁺. (**B**) i) Representative histograms of PDPN gMFI for mGFP⁺ and LEC populations (ii)

gMFI for PDPN in mGFP$^+$ (fibroblasts) and LECs. N>8 mice for each genetic model. Mann-Whitney test (two tailed), ****p<0.0001, ns = not significant. (**C**) UMAP plot of fibroblasts (CD45$^-$CD31$^-$) and (**D**) heatmap showing DEGs. Ratio of Control (blue) and ΔPDPN (pink) numbers (top row). (**E**) Contour density plots of Control versus ΔPDPN fibroblasts (CD45$^-$CD31$^-$). (**F**) Neighbourhood distance analysis (MiloR) showing Control (blue gradient) or ΔPDPN (red gradient) enriched areas.

ΔPDPN FRCs are transcriptionally distinct from Control FRC subsets

We more closely examined cells clustering in the *Nr4a1* and *Ccl19*^{hi} subsets which were enriched in ΔPDPN lymph nodes. We performed subclustering analysis (Seurat) and found shifts within transcriptional states. For example, within the *Nr4a1* cluster, we found more (80.1:19.9 ratio) ΔPDPN cells in the *Ccl21*^{hi} subcluster and reduced numbers (20.3:79.7 ratio) of ΔPDPN in the *Ccl21*^{lo} subcluster (Fig. 2,A and B, and table S4,).

When we examined the *Ccl19*^{hi} subset, subclustering analysis revealed an enrichment of ΔPDPN FRCs in a *Tnc*^{hi} subcluster (87.4:12.6 ratio) (Fig. 2,C and D, and table S5). To validate these data, we immunostained lymph nodes from PDGFRα^{mGFP} and PDGFRα^{mGFPΔPDPN} mice and quantified a >30% increase in Tenascin C (TNC) protein expression in PDGFRα^{mGFPΔPDPN} tissues (Fig. 2,E and F) which correlated with the increased overall expression of *Tnc* quantified across all fibroblast subsets in the scRNA-seq data (Fig. 2G). Since Tenascin C is highly linked to inflammatory states (*45*, *46*), we performed DAVID analysis to compare inflammatory pathways between Control and ΔPDPN fibroblasts (Fig. 2H). We found enrichment of biological pathways relating to cell and matrix adhesion and upregulation of many NF-κB target genes in ΔPDPN fibroblasts (Fig. 2,H and I). Interestingly, NF-κB signalling, downstream of lymphotoxin-β receptor engagement, has been implicated in FRC development (*47*). *Ptgs2,* encoding COX-2, a key enzyme to produce inflammatory prostaglandins (*48*), is positively regulated by NF-κB and is enriched in ΔPDPN fibroblasts (Fig. 2,I and J). COX-2 expression by FRCs has been linked suppression of T cell activation in lymph nodes (*49*). We tested whether Podoplanin impacted COX-2 expression at protein level in FRC cell lines *in vitro,* using shRNA to knockdown PDPN expression, and confirmed by western blotting upregulation of COX-2 in PDPN KD cell lines (Fig. 2K). We therefore link Podoplanin directly and intrinsically to NF-κB signalling and COX-2 expression in FRCs.

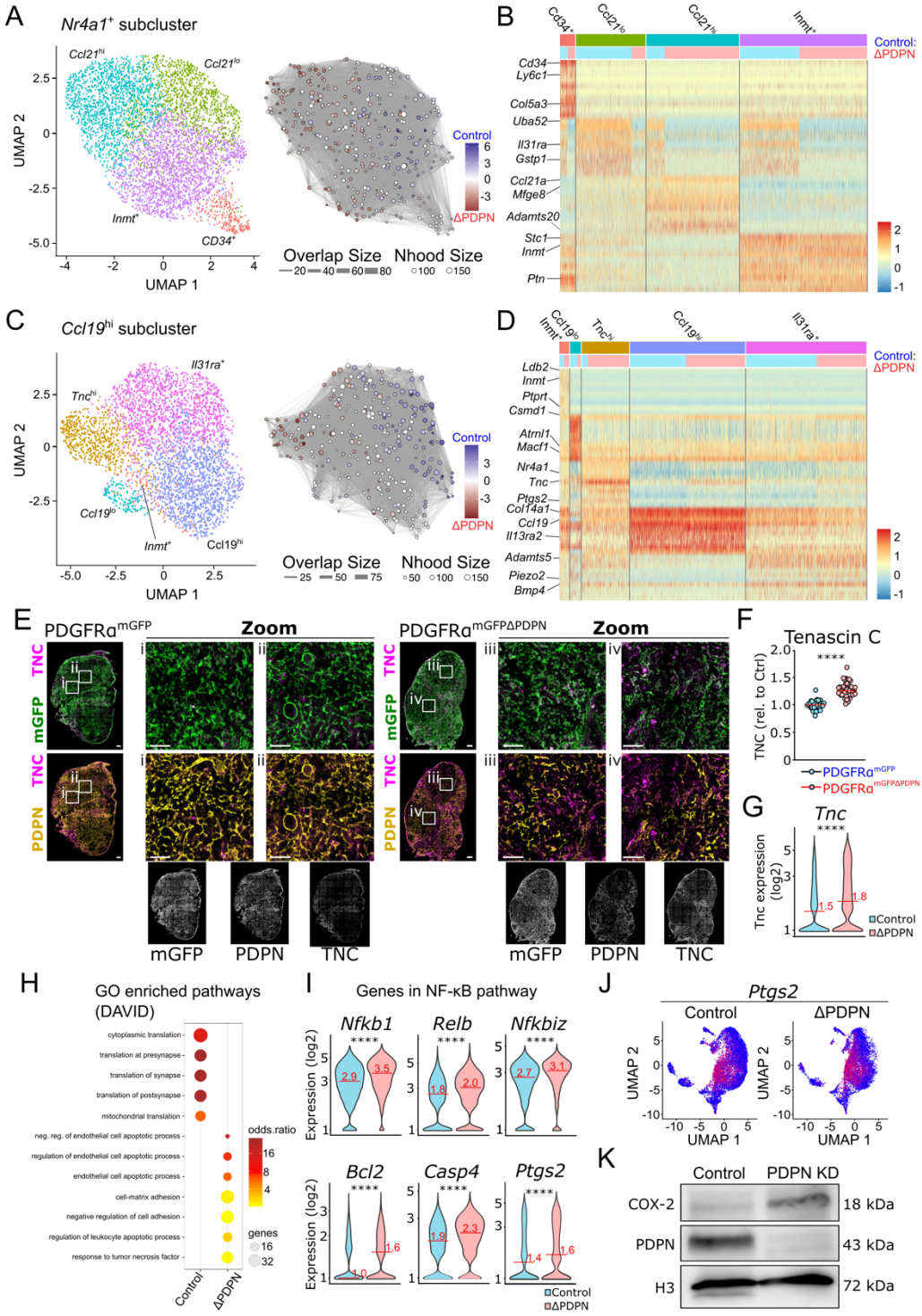

Fig. 2. Distinct transcriptional profile in PDGFRα$^{mGFP\Delta PDPN}$ fibroblasts. (**A**) Subcluster analysis of *Nr4a1*$^{+}$ cluster, miloR showing PDGFRα^{mGFP} (Control -blue gradient) and PDGFRα$^{mGFP\Delta PDPN}$ (ΔPDPN -red gradient) enriched areas. (**B**) Heatmap showing top 10 DEGs for each defined subcluster, Ratio of Control (blue) and ΔPDPN (pink) numbers (top row). (**C**) Subcluster analysis of *Ccl19*^{hi} cluster and miloR showing PDGFRα^{mGFP} (Control -blue gradient) and ΔPDPN (red gradient) enriched areas. (**D**) Heatmap showing top 10 DEGs for each defined subcluster. Ratio of Control (blue) and ΔPDPN (pink) numbers (top row). (**E**) Tilescans and zoomed areas comparing PDGFRα^{mGFP} and PDGFRα$^{mGFP\Delta PDPN}$ lymph nodes (mGFP -green), Podoplanin (PDPN

– yellow) and Tenascin C (TNC – magenta). (**F**) Quantification of TNC immunofluorescence representative of 4-5 lymph nodes per condition. Scales bar = 50 μm. (**G**) Violin plot showing *Tnc* expression PDGFRα^{mGFP} and PDGFRα$^{mGFP\Delta PDPN}$ fibroblasts from scRNA-seq analysis. (**H**) GO-enriched pathways (DAVID) in PDGFRα^{mGFP} and PDGFRα$^{mGFP\Delta PDPN}$ fibroblasts. (**I**) Violin plots with median expression for NF-κB pathway genes: *Nfkb1*, *Relb*, *Nfkbiz*, *Bcl2*, *Casp4* and *Ptgs2*. Mann-Whitney test (two tailed), ****$p<0.0001$. (**J**) Expression of *Ptgs2* on fibroblast UMAP. (**K**) Western blot for COX-2, PDPN and Histone H3 in FRC cell lines, control versus shRNA KD PDPN (PDPN KD).

Lymph node network integrity and FRC inflammatory profile altered by Podoplanin

Since our analysis highlighted the cell-matrix adhesion GO term as enriched in ΔPDPN FRCs (Fig. 2H), we next asked if other matrix components were altered in PDGFRα$^{mGFP\Delta PDPN}$ lymph nodes. Tilescans showed increased deposition of perlecan, a basement membrane component, in PDGFRα$^{mGFP\Delta PDPN}$ lymph nodes (Fig. 3A) which confirmed that matrix remodelling is widely impacted by Podoplanin deletion. We observed areas of the paracortex tightly packed with leukocytes (nuclei stained with DAPI) but devoid of GFP^{+} fibroblasts in PDGFRα$^{mGFP\Delta PDPN}$ mice. These areas also lacked extracellular matrix components of the conduit network suggesting that the reticular network had lost integrity (Fig. 3A). To quantify the disruption of the FRC network in the paracortex we used an ImageJ tool (Mitochondrial Network Analysis - MiNA) based on 'skeletisation' to quantify mathematical properties of the network (Fig. 3,B and C) (*50*). We find in PDGFRα$^{mGFP\Delta PDPN}$ mice there is a 60% decrease in the number of branches, shortened branch length and a 25% decrease in the network footprint, confirming a severe disruption to the FRC network (Fig. 3,B and C).

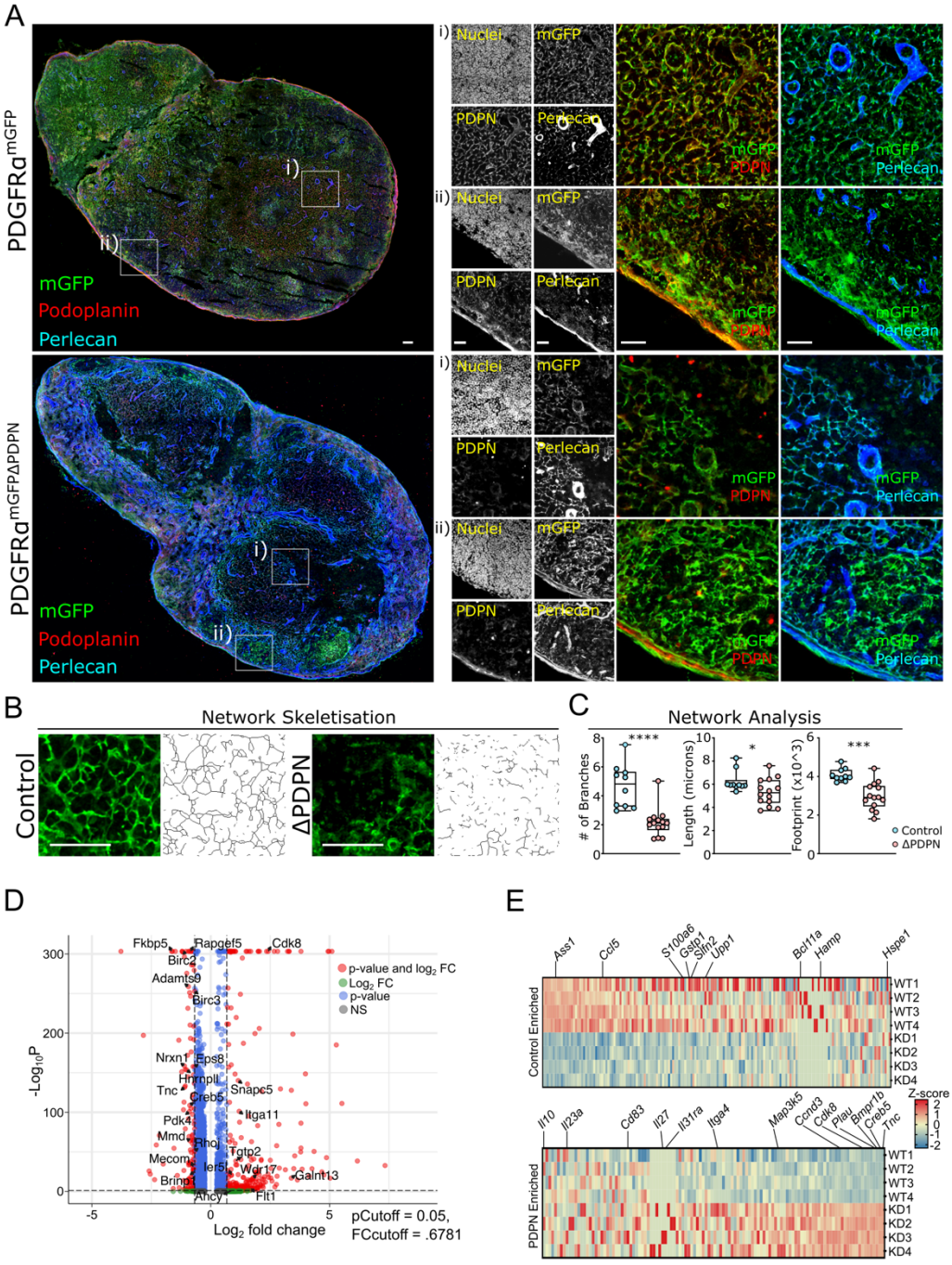

Fig. 3. Lymph node network integrity and FRC inflammatory profile altered by Podoplanin

(A) Representative tilescan of PDGFRα^{mGFP} (Control) or PDGFRα$^{mGFP\Delta PDPN}$ (ΔPDPN) lymph nodes. Staining for Podoplanin (red), mGFP (green) and perlecan (blue); zoomed images of (i) paracortex (T cell area) (ii) capsule. Scale bar = 50 μm. **(B)** Representative images of FRC network (mGFP) and network skeletisation for PDGFRα^{mGFP} (control) or PDGFRα$^{mGFP\Delta PDPN}$ (ΔPDPN) lymph nodes. Scale bar = 100 μm. **(C)** Network analysis quantifying the number of network branches, length of branches and network footprint. Network quantification N=10-15 ROI of lymph node paracortex; Mann-Whitney test (two tailed), ****p<0.0001, ***p<0.001, *p<0.05. **(D)** Volcano plot showing genes significantly altered after PDPN deletion

206 (scRNA-seq dataset). **(E)** DEGs from (D) overlaid with *ex vivo* bulk RNA-seq of FRC cell lines expressing basal levels control
207 versus shRNA KD PDPN (PDPN KD).
208
209 The scRNA-seq data provide evidence that Podoplanin expression by FRCs is important for
210 determining their transcriptional state, which impacts their subset identity (Fig. 1 and 2). However,
211 the transcriptional changes *in vivo* could be caused by a combination of cell intrinsic mechanisms and
212 by alterations in crosstalk between other tissue cell types. To address how the Podoplanin intrinsically
213 regulates gene expression in FRCs, we silenced Podoplanin expression in FRC cell lines *in vitro* and
214 performed bulk RNA-seq. This dataset provides a robust, reproducible readout of average cell state
215 therefore highlights genes regulated by Podoplanin which are not dependent on the tissue
216 microenvironment. We compared a list of 403 genes significantly altered by Podoplanin expression
217 across all *in vivo* cell clusters to our bulk RNA-seq analysis (Fig. 3D). Of these, 290 were also found in
218 our the Podoplanin -dependent gene signatures *in vitro* (Fig. 3E, and table S6). Interestingly, many of
219 these genes directly regulated by Podoplanin expression were targets of NF-κB as predicted by the
220 DAVID analysis of our *in vivo* data (Fig. 2H). Of note, *Tnc* was upregulated across multiple stromal
221 subsets in the scRNA-seq data, validated in tissue staining at protein level and indeed also upregulated
222 in PDPN-KD FRC cell lines *in vitro*. Upregulation of *Plau* (Fig. 3E), another gene inversely correlated
223 with Podoplanin expression, has been linked conversion of fibroblasts to inflammatory-type cancer
224 associated fibroblasts in oesophageal SCC (*51*). On the other hand, downregulation of *Ass1* (Fig. 3E) is
225 linked to pulmonary fibrosis (*52*). We therefore conclude that Podoplanin can directly and intrinsically
226 impact the inflammatory state of FRCs.
227
228 **PDPN/CLEC-2 signalling induces two distinct transcriptional signatures**
229 While we show that Podoplanin can directly change the phenotype of FRCs *in vivo* and *in vitro*, FRCs
230 also have important crosstalk with neighbouring immune cells. Podoplanin is a membrane
231 glycoprotein that can bind and cluster with CLEC-2 (*53*), a C-type lectin expressed on migratory DCs,
232 platelets and other myeloid cells (*27*, *54*). We exploited the *in vitro* FRC cell lines to directly test the
233 effect of CLEC-2 engagement and compare immediate (6 hour) and longer-term (24 hours)
234 transcriptional changes to FRCs (Fig. 4). Using this experimental set up we were able to isolate genes
235 that were intrinsically Podoplanin-dependent and importantly were unaffected by ligand binding (Fig.
236 4A, and table S7). The Podoplanin-dependent upregulated genes included fibroblast markers (*Thy1*),
237 vesicular transport and autophagy (*Atg3, Atg12, Pink1, Lamp2, Dnm1, Tapb2*), cell signalling (*Jak2,*
238 *Gatsl3, Dusp16*), actin dynamics (*Rnd1, Ssh3*), and transcription factors (*Sox11, Ahr, Hoxd9, Cxxc5*) (fig.
239 S3A).
240

241 When we examined the genes transcriptionally regulated after treatment with CLEC-2 (Fig. 4B, and
242 table S7), we observed most differentially expressed genes occurred at 6 hours (Fig. 4B). This finding
243 supports previous knowledge that CLEC-2 signalling is transient in FRCs (*34*). It has been previously
244 reported that signalling of Podoplanin to cytoskeletal modulators is dampened by binding of CLEC-2
245 (*6*) and exposing FRCs to CLEC-2 phenocopies a loss of Podoplanin through reduction in actomyosin
246 contractility (*6*). Therefore, we asked whether CLEC-2-upregulated genes correlated with PDPN KD.
247 Hierarchical clustering revealed four PDPN and CLEC-2-dependent groups (Fig. 4B). The two largest
248 clusters were downregulated by CLEC-2 at 6 hours (including the Wnt ligands *Wnt4* and *Wnt7b*, and
249 the extracellular matrix components *Tnn* and *Prg4*) and only a small fraction of these genes followed
250 the previously reported pattern phenocopying PDPN KD (Fig. 4B). We found only a small fraction of
251 hits (85 and 236 genes), overlap between the genes regulated by Podoplanin or CLEC-2 (fig. S3A)
252 suggesting that while in some cases CLEC-2 binding does phenocopy loss of Podoplanin expression,
253 CLEC-2 also induces a distinct transcriptional signature (Fig. 4C).

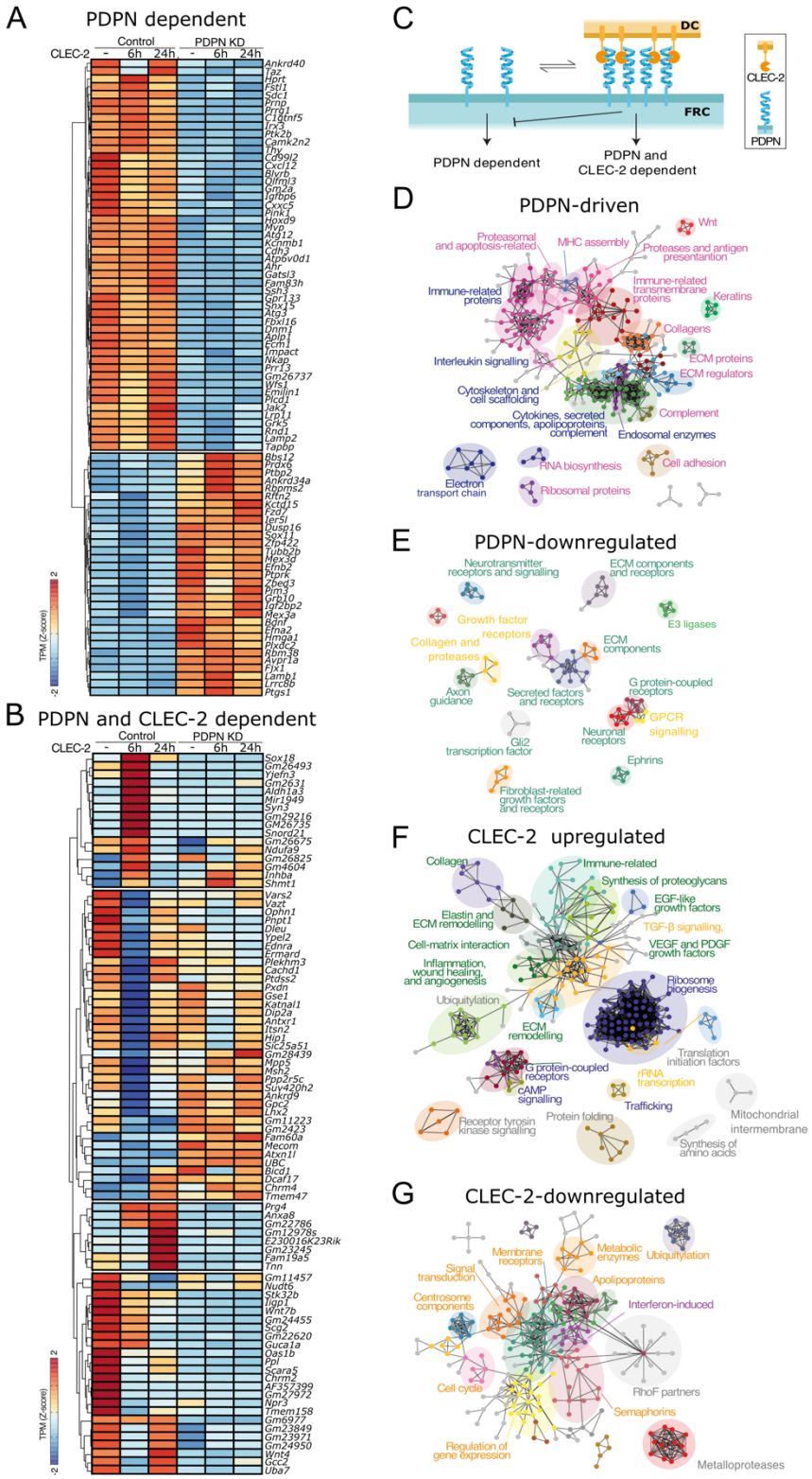

Fig. 4. PDPN/CLEC-2 signalling axis controls the transcriptional landscape of FRCs *ex vivo*. (**A**) Heatmap of the genes regulated by PDPN expression independently of CLEC-2 signalling. (**B**) Heatmap of the genes regulated by CLEC-2 in PDPN$^+$ (Control) FRC cell line. (**C**) Diagram of proposed modes of transcriptional regulation. (**D**) STRING analysis of PDPN-driven, (**E**) PDPN-downregulated, (**F**) CLEC-2 upregulated and (**G**) CLEC-2 downregulated genes.

260 We used the STRING functional annotation platform to study functional networks, including physical
261 interactions as well as functional connections (Fig. 4,D to G). PDPN-driven genes formed a large cluster
262 of immune-related genes (Fig. 4,D and E, and table S8). This cluster included membrane receptors
263 (*Cd47*, *Itgb2*), cytokine signalling (*Stat1*, *Stat2*, *Irf7*, *Fit1*, *Ifit1*, *Ifit3*, *Cxcl1, Cxcl10, Cxcl5, Ccl2, Ccl9*),
264 several collagen genes, ECM components (*Ecm1, Timp3*) consistent with early microarray analysis of
265 lymph node stromal cells (*40*), complement genes (*C2, C3, C1ra, C1s1, C1s2*), and genes related to
266 antigen presentation (*Anpep, H2-T23, H2-K1*). CLEC-2 regulated genes formed a large cluster of hits
267 related to ribosome biogenesis and regulation of translation (Fig. 4,F and G, and table S8). Moreover,
268 in line with the PDPN-driven genes, we found clusters associated to immune-related functions and
269 signalling, including different families of growth factors (*Tgfb*, *Vegf*, *Pdgf*), genes involved in
270 inflammation, wound healing, and angiogenesis. Moreover, PDPN expression and CLEC-2 binding
271 altered expression of many transcription factors which would be expected to have wide ranging
272 effects on the transcriptional profile of FRCs (fig. S3,B and C). We performed gene-enrichment analysis
273 using the GO Biological Process (http://genontology.org) database and found that PDPN-driven
274 pathways included response to mechanical stimuli and extracellular matrix organisation as have been
275 previously reported (*8*, *34*) (fig. S3,D to G), but which we can now also confirm *in vivo* in our scRNA-
276 seq analysis (Fig. 2).
277
278 **Stromal/immune cell crosstalk is altered in PDGFRα$^{mGFP\Delta PDPN}$ lymph nodes**
279 To examine the impact of stromal PDPN deletion on immune cell crosstalk in tissues we quantified
280 immune cell populations in PDGFRα^{mGFP} and PDGFRα$^{mGFP\Delta PDPN}$ lymph nodes (fig. S1B). CD45^{+} and CD31^{+}
281 cells (immune and endothelial cells) were enriched from Control and PDGFRα$^{mGFP\Delta PDPN}$ lymph nodes
282 (fig. S1B). We identified 21 clusters of immune and endothelial cells with distinct transcriptional
283 profiles (Fig. 5A and B, fig. S4, table S9). Neighbourhood analysis by miloR showed a loss of myeloid
284 cells, macrophages, B cells and CD4^{+} T cells in PDGFRα$^{mGFP\Delta PDPN}$ (blue neighbourhoods) (Fig. 5C).

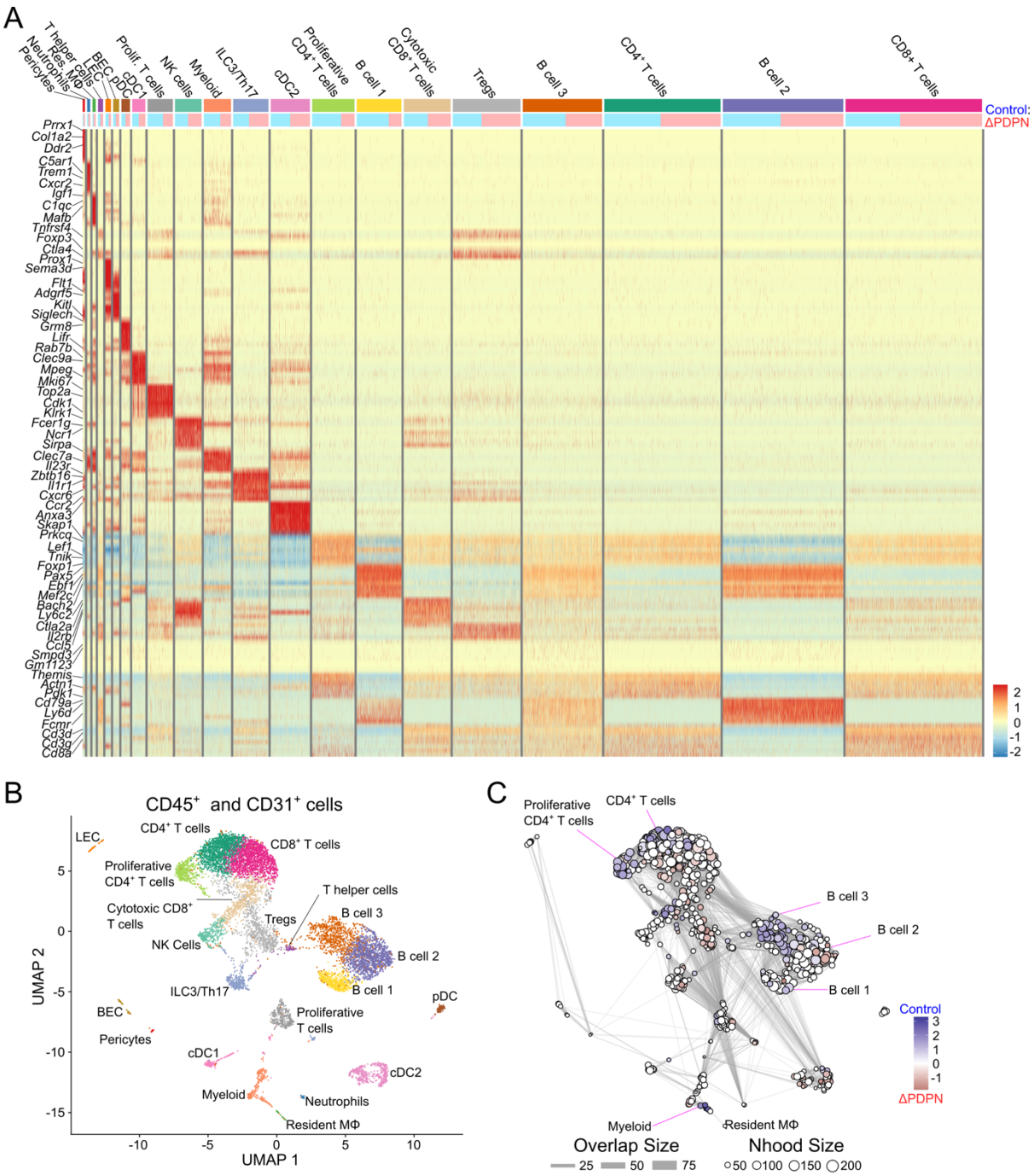

Fig. 5. Immune cell transcriptional profile is altered by Podoplanin deletion. (**A**) Heatmap analysis of immune and endothelial clusters (**B**) UMAP and (**C**) MiloR neighbourhood analysis showing Control (blue gradient) and ΔPDPN (red gradient) abundant areas.

Stromal cross talk with innate immune cells is reduced in the absence of Podoplanin

To understand how the crosstalk between immune cells and stromal cells is affected we performed CellChat analysis between stromal and immune populations (fig. S5) (*55*, *56*). Many of the enriched pathways in the PDGFRα$^{mGFP\Delta PDPN}$ lymph nodes support a proinflammatory profile, including RANKL, TENASCIN, TGFb, and CXCL (fig. S5A). We examined both the number of interactions (fig. S6B), and

295 the interaction strength (fig. S5C) between stromal cells and immune cells. Our data show that
296 interactions between stromal cells and myeloid cells were particularly attenuated in PDGFR$\alpha^{mGFP\Delta PDPN}$
297 lymph nodes; whereas interactions between stromal cells and cDC2 cells were actually enhanced after
298 Podoplanin deletion (fig S5B and C).
299
300 Past studies have also shown the importance of CLEC2:PDPN signalling in driving dendritic cell
301 migration and lymph node activation during immune responses (*6*). We also find CLEC-2 dependent
302 transcriptional regulation through PDPN (Fig. 4). We therefore performed subcluster analysis on the
303 myeloid and resident macrophage populations, and dendritic cells (Fig. 6,A and B, and tables S11 and
304 12). We observed a reduction in the number of inflammatory monocytes/macrophages in
305 PDGFR$\alpha^{mGFP\Delta PDPN}$ lymph nodes, however there was an enrichment in the monocyte derived
306 macrophage cluster (red gradient) (Fig.6,A and B). We also performed subcluster analysis on all DC
307 clusters: cDC1, cDC2 and pDCs (Fig. 6,C and D, and table S12). Neighbourhood analysis revealed shifts
308 in within the cDC2 subclusters with *Ccl5*^{hi} cDC2 being enriched in Control tissues (Blue) whereas *Nrp2*$^{+}$
309 cDC2 were enriched in PDGFR$\alpha^{mGFP\Delta PDPN}$ tissues (Red) (*57*). To validate these transcriptomic data, we
310 examined myeloid cells by flow cytometry and microscopy (Fig. 6,E and F, and fig. S6). In
311 PDGFR$\alpha^{mGFP\Delta PDPN}$ lymph nodes we observed a reduction of CD103^{+} DC and but an increase in the
312 percentage of Ly6c^{hi} Monocytes (Fig. 6D). We compared numbers and location of CD11b^{+} cells in lymph
313 node tissue sections and observed reduced CD11b^{+} cells in PDGFR$\alpha^{mGFP\Delta PDPN}$ lymph nodes (Fig. 6,G and
314 H). The CD11b^{+} cells in PDGFR$\alpha^{mGFP\Delta PDPN}$ lymph nodes were also more circular, which is consistent with
315 the increased number of monocytes (Fig. 6,G and H). Overall, this suggests that in addition to affecting
316 the transcriptional state of fibroblasts, PDPN deletion also affects the activation state and cellular
317 composition of myeloid cells in the lymph node at steady-state.

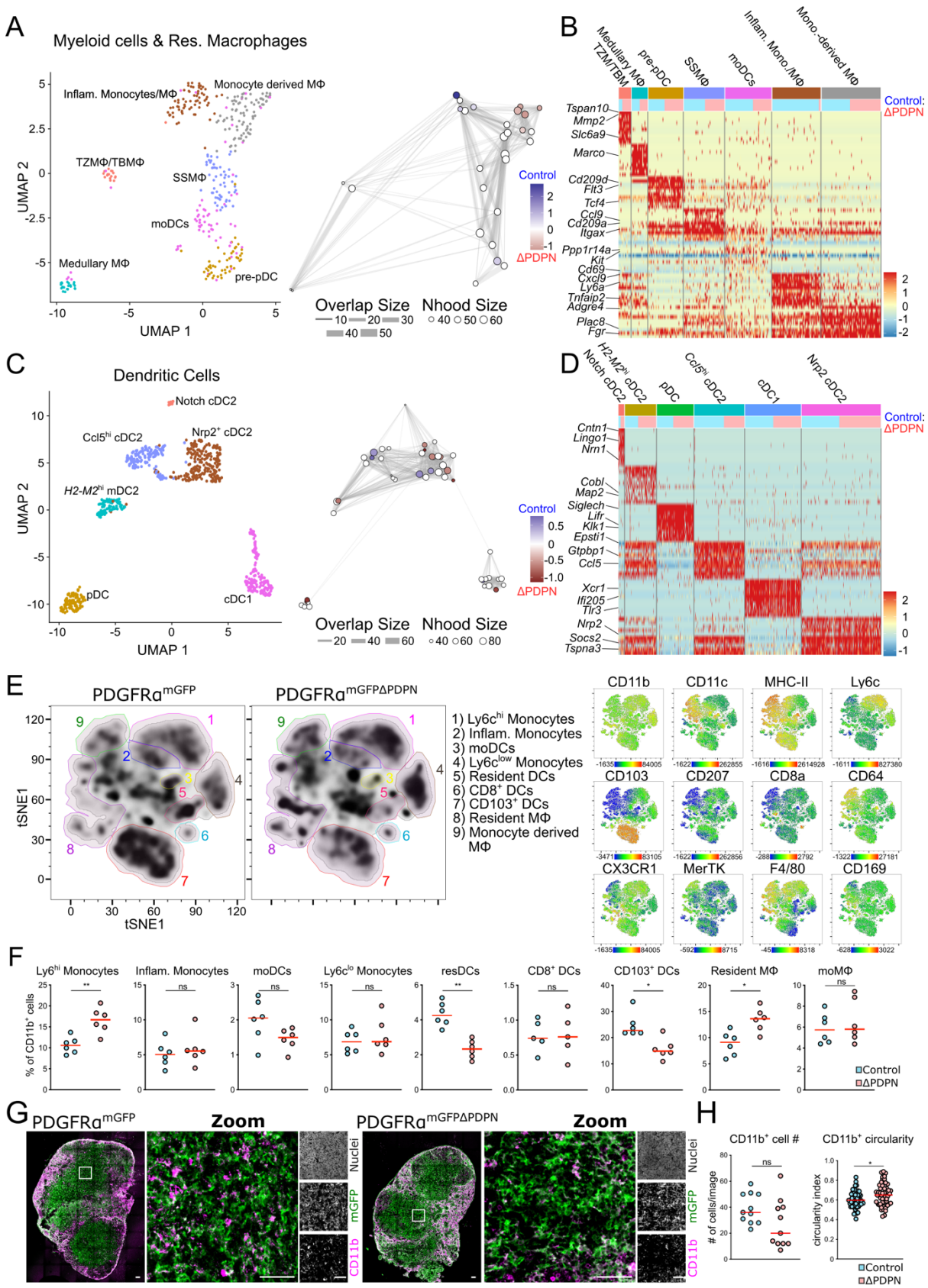

Fig. 6. Innate cell phenotype and numbers altered in PDGFRα$^{mGFP\Delta PDPN}$ lymph nodes. (**A**) Subcluster analysis of Myeloid & Resident Macrophages showing UMAP, MiloR neighbourhood distance analysis (**B**) Heatmap of DEGs of Myeloid & Resident Macrophages. **(C)** Subcluster analysis of Dendritic cells (cDC1, cDC2 and pDC clusters) showing UMAP, MiloR neighbourhood

322 distance analysis **(D)** Heatmap DEGs for dendritic cell populations. **(E)** Flow cytometry analysis of innate immune cells
323 ($CD45^+CD11b^+$), tSNE plots using the markers: CD11c, I-A/I-E (MHC-II), Ly6c, CD103, CD207, CD8a, CD64, CX3CR1, MerTK,
324 F4/80 and CD169. (**F**) Changes in the percentages of each innate cell population comparing Control and ΔPDPN. Mann-
325 Whitney test (two tailed), ns = no significance, **p<0.01, *p<0.05. (**G**) Tilescans of PDGFRα^{mGFP} and PDGFR$\alpha^{mGFP\Delta PDPN}$ lymph
326 nodes stained for mGFP (green) and CD11b (magenta) **(H)** Quantification of number of $CD11b^+$ cells per ROI and circularity
327 index of each $CD11b^+$ cell. Scale bar = 50 μm. Images representative of 4-5 lymph nodes for each genetic model Mann-
328 Whitney test (two tailed), ns = no significance, *p<0.05
329

330 **Disrupted stromal-immune crosstalk in PDGFR$\alpha^{mGFP\Delta PDPN}$ mice attenuates B cell activation**

331 In addition to reduced crosstalk with innate cells, we also observed changes to B cell populations in
332 PDGFR$\alpha^{mGFP\Delta PDPN}$ lymph nodes (Fig. 5). We performed subcluster analysis of B cell populations to
333 understand how Podoplanin deletion affects their phenotype (Fig. 7A, and table S12). MiloR analysis
334 shows altered neighbourhood clusters and there were fewer activated or germinal centre-like B cells
335 in PDGFR$\alpha^{mGFP\Delta PDPN}$ lymph nodes (Fig. 7,A and B). B cell follicles are supported by a stromal network of
336 FDCs which are a distinct subset of stromal cells that specifically support B cells through the production
337 of CXCL13 for their recruitment, and growth factors such as BAFF (*13*, *17*). FDCs also form the stromal
338 scaffolds for germinal centre (GC) formation and retain and present antigen to B cells to support B cell
339 selection (*58*). Since FDCs are of mesenchymal origin and express PDGFRα (*13*) they also conditionally
340 targeted in our PDGFR$\alpha^{mGFP\Delta PDPN}$ mice. FDCs also express PDPN (fig. S2), although at lower levels than
341 FRCs, but the function of PDPN in FDCs has not previously been investigated. To understand why B
342 cell populations would be affected by Podoplanin deletion, we next performed subcluster analysis of
343 the stromal cells supporting B cell function, FDCs (Fig. 7C) and MRCs (Fig 7D), (fig. S7,A and B, and
344 tables S13 and S14). In PDGFR$\alpha^{mGFP\Delta PDPN}$ lymph nodes miloR analysis highlighted shifts in FDCs cluster
345 towards reduced expression of *Fcgr2b*, which would be consistent with reduced activation of B cells
346 (Fig. 7A, fig. S7A, and table S13). In tissues, we measured the area covered by the FDC network in each
347 B cell follicle (fig. S7C) and found a similar number of B cell follicles and FDC network size between
348 PDGFRα^{mGFP} and PDGFR$\alpha^{mGFP\Delta PDPN}$ mice. However, the follicle size was slightly reduced in the latter
349 (fig. S7C). The MRC subcluster analysis also revealed a shift towards MRCs expressing *Nr4a1* in
350 PDGFR$\alpha^{mGFP\Delta PDPN}$ mice (Fig. 7D, fig. S7B, and table S14). Interestingly, the PDGFR$\alpha^{mGFP\Delta PDPN}$ MRC
351 populations also showed higher expression of inflammatory pathways such as *Ptgs2, Cxcl1,* similarly
352 to TRC populations (fig. S7D, and Fig. 2). Overall, these findings show that Podoplanin drives changes
353 in the phenotype of FDCs and MRCs which could compromise the crosstalk with B cells.
354

355 The defect in B cell activation could be a direct intrinsic defect, a failure of T cell help or insufficient
356 stromal cell support. We therefore examined if the deletion of PDPN alters adaptive immune

357 responses *in vivo* after immunisation. We compared early activation (day 5) and later stages (day 9)
358 (fig. S8). PDGFR$\alpha^{mGFP\Delta PDPN}$ lymph nodes expanded less than controls (fig. S8). We have shown
359 previously that PDPN is a mechanical sensor in FRCs and is required to trigger FRC proliferation in
360 response to increased mechanical strain as the lymph node begins to expand (*8*). To specifically
361 quantify how B cell activation is affected by Podoplanin deletion we also measured antibody responses
362 in the serum 28 days post immunisation. We found that PDGFR$\alpha^{mGFP\Delta PDPN}$ mice had reduced levels of
363 antigen (ovalbumin) specific IgG1, IgG2a and IgE in the serum (Fig. 7,E to H), thereby confirming that
364 Podoplanin deletion has a significant functional impact on adaptive immune responses. Tissue analysis
365 of immunised mice showed there is a trend towards fewer GCs per lymph node in PDGFR$\alpha^{mGFP\Delta PDPN}$
366 mice, and those GCs present tend to be smaller (Fig. 7,I and J). This results in altered structure of GCs
367 in PDGFR$\alpha^{mGFP\Delta PDPN}$ mice as measured by an increased ratio (>2 fold) of FDC to GC area (Fig. 7J)
368 suggesting that there may be a difference in the functional capacity of FDC in PDGFR$\alpha^{mGFP\Delta PDPN}$ LNs to
369 support B cell activation and that PDPN also plays a role in FDC specification and function.
370
371 Overall, our data show that Podoplanin regulates the transcription profile of FRCs in addition to
372 controlling cellular mechanics and actomyosin contractility. Loss of Podoplanin broadly upregulates
373 expression of inflammatory molecules and pathways which will impact many different immune cell
374 types and the overall immunoregulatory functions of the lymphoid tissues.
375
376

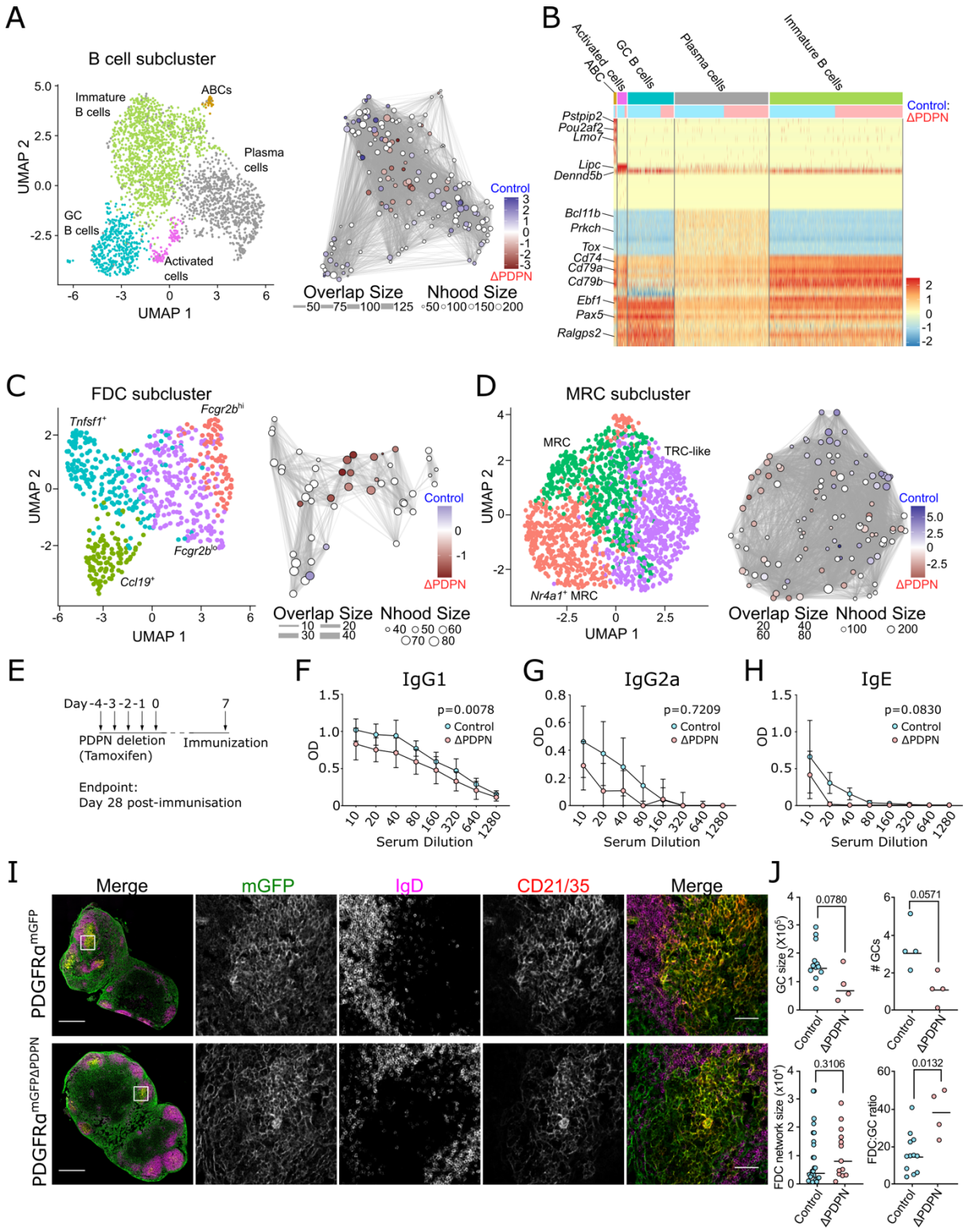

Fig. 7. B cell function during steady-state and inflammation compromised by Podoplanin deletion

(**A**) B cell subcluster UMAP and MiloR showing PDGFRα^{mGFP} (Control -blue gradient) and PDGFRα$^{mGFP\Delta PDPN}$ (ΔPDPN -red gradient) enriched areas. (**B**) Heatmap showing top 10 DEGs for each defined subcluster, ratio of Control (blue) and ΔPDPN (pink) numbers (top row). (**C**) FDC and (**D**) MRC subcluster UMAP and MiloR showing PDGFRα^{mGFP} (Control -blue gradient) and ΔPDPN (red gradient) enriched areas. (**B**) Heatmap showing top 10 DEGs for each defined subcluster, ratio of Control (blue) and ΔPDPN (pink) numbers (top row). (**E**) Schematic of experimental design for immunisation (IFA-OVA) after Podoplanin deletion. Ovalbumin-specific (**F**) IgG1, (**G**) IgG2a and (**H**) IgE in serum from PDGFRα^{mGFP} (Control) and

385 PDGFR$\alpha^{mGFP\Delta PDPN}$ (ΔPDPN). Wilcoxon test, p-values indicated. (**I**) Tilescans of PDGFRα^{mGFP} and PDGFR$\alpha^{mGFP\Delta PDPN}$ lymph nodes
386 stained for mGFP (green), IgD (magenta) and CD21/35 (red). (**J**) Analysis of germinal centre (GC) size, GC number FDC network
387 size and ratio of FDCs to GCs. Mann-Whitney test (two tailed), p-values indicated. Scale bar = 500 μm and 50 μm in zoomed
388 images. Images representative of 4-5 lymph nodes for each condition from 2 independent experiments.
389

390 **DISCUSSION**

391 Podoplanin has complex functions which until now have only been partially described. Podoplanin
392 was first described as a ligand for DC trafficking (*27*) but has since been shown to also maintain HEV
393 integrity through crosstalk with platelets (*54*), regulate extracellular matrix deposition (*34*) and to
394 control the contractility (*6*, *7*) and tissue tension (*8*) of the FRC network. Podoplanin acts as a
395 mechanical sensor in FRCs to trigger proliferation and lack of Podoplanin in FRCs attenuates the acute
396 phase of lymph node expansion (*8*). Now, we show that Podoplanin regulates FRC transcriptional
397 programmes and cell state in both tissue contexts and intrinsically in simple *in vitro* cell systems.
398 Broadly, loss of Podoplanin expression induced upregulation of the NF-κB signalling pathway and
399 expression of pro-inflammatory molecules. For example, COX-2 driving prostaglandin expression (*59*,
400 *60*) and Tenascin C which is a proinflammatory matrix protein normally associated with wound
401 healing, myofibroblast activation and fibrosis (*45*, *46*). In the lymph node, these transcriptional shifts
402 led to reduced numbers of *Cxcl9*$^{+}$, *Ccl19*$^{+}$ and *Ccl21*$^{+}$ TRC subsets and an enrichment of FRCs expressing
403 *Nr4a1*, a subset previously associated with early activation markers (*13*). This pro-inflammatory
404 change in inflammatory state *in vivo* may have been caused by crosstalk between stromal cells and
405 immune cells, however a significant proportion of this transcriptional shift was also observed in bulk
406 RNA-seq analysis *in vitro* using immortalised FRC cell lines, meaning that Podoplanin was directly and
407 intrinsically affecting the phenotype of lymph node fibroblasts. We further tested how the
408 PDPN/CLEC-2 signaling axis impacted the immunoregulatory properties of FRCs *in vitro* and *in vivo,*
409 which revealed that Podoplanin expression in fibroblastic stroma instructs a second, ligand-
410 dependent, transcriptional programme that drives extensive alterations in gene expression in FRCs.
411
412 Podoplanin-dependent FRC phenotypes impacted immune cell function in steady state and in reactive
413 lymph nodes. In PDGFRα$^{mGFP\Delta PDPN}$ lymph nodes the crosstalk between stromal cells and myeloid cells
414 such as macrophages and monocytes were negatively impacted. We found reduced numbers of
415 myeloid cells and dendritic cell subsets in PDGFRα$^{mGFP\Delta PDPN}$ lymph nodes by flow cytometry and tissue
416 staining. Interestingly, B cell function was also dependent on Podoplanin expression on lymph node
417 stroma (FDC and MRC). We found structural changes to B cell follicles in PDGFRα$^{mGFP\Delta PDPN}$ lymph nodes
418 in steady state which then impacted B cell activation, germinal centre formation and antibody class
419 switching. These data suggest that Podoplanin has important roles in FDCs in additional to TRCs which
420 has not previously been reported.
421
422 Podoplanin is expressed by lymphoid tissue fibroblasts from early in development. The interaction
423 between CLEC-2 and Podoplanin is required for the development and maintenance of lymph nodes

424 (*39*). Indeed, lymph nodes do not develop in a full knockout of Podoplanin (*37*). In contrast, FRCs in
425 aged lymph nodes exhibit impaired upregulation of Podoplanin making them less able to respond to
426 immune challenges (*61*). Beyond secondary lymphoid tissues, PDPN positive stromal cells are key for
427 the early support of tertiary lymphoid structure development (*62*) building the case that Podoplanin
428 is essential for the immunoregulatory properties of lymphoid tissue associated stroma at all life stages.
429
430 Podoplanin expression in lymph node stroma is notably altered in a variety of pathological states. For
431 example, lymph nodes from diffuse large B cell lymphoma (DLBCL) patients show upregulation of
432 Podoplanin which is associated with increase stromal density, immunosuppression of $CD8^+$ cytotoxic
433 T cells and immune evasion of lymphoma B cells (*63*). This change in stromal phenotype correlated
434 with reduced adaptive immune function, and a decrease in germinal centre formation.
435
436 Fibroblastic stroma is also ubiquitous across diverse tissues (*9*). Fibroblast populations are specifically
437 adapted to the functional requirements of their tissue microenvironments (*42*, *64*, *65*). Fibroblasts are
438 also remarkably plastic, able to change their phenotype and function in response to inflammation or
439 tissue damage (*65*, *66*). Here we have studied Fibroblastic reticular cells of lymph nodes which are the
440 archetype immunoregulatory fibroblast. However, how fibroblasts such as TRCs acquire
441 immunoregulatory functions is not well understood (*2*, *3*). Immunoregulatory fibroblasts can also exist
442 outside of lymphoid tissues. For example, both mouse and human tissue studies indicate that some
443 cancer-associated fibroblasts acquire inflammatory phenotypes and can alter immune function in
444 tumours (*66*). $PDPN^+$ fibroblasts also spontaneously develop in a wide variety of inflammatory
445 conditions (*21*). Our data confirms the importance of Podoplanin in the functional phenotype of FRCs,
446 and the role of Podoplanin in inflammatory transcriptional signatures. These data lead us to propose
447 that Podoplanin expression is fundamental to FRC function in lymph nodes and may determine the
448 immunoregulatory properties of fibroblasts more widely across other tissues and pathologies.

449 **MATERIALS AND METHODS**

450 **Mice**

451 Experiments were performed in accordance with national and institutional guidelines for animal care
452 and approved for the Laboratory for Molecular and Cell Biology by the institutional animal ethics
453 committee review board, European research council, and the UK Home office. Breeding of animal lines
454 were maintained at Charles River Laboratory. For generation of the *Pdgfra*-mGFP-CreERT2 and *Pdgfra*-
455 mGFP-CreERT2 x *Pdpn*$^{fl/fl}$ refer to Horsnell et al., 2022 (*8*). Females and males aged between 8 and 13
456 weeks were used for experiments, unless stated otherwise.

457

458 **Tamoxifen administration**

459 Activation of the Cre recombinase was achieved through the administration of tamoxifen (22 mg ml−1;
460 Sigma-Aldrich) resuspended in corn oil (Sigma-Aldrich) or sunflower oil (Sigma-Aldrich). Tamoxifen
461 was dosed (82 μg g−1) intraperitoneally on 3 consecutive days or by gavage for 5 consecutive days.
462 For immunisation experiments, mice were immunised 7 days after tamoxifen treatment. For steady-
463 state experiments mice were sacrificed 10 days after tamoxifen treatment. Inguinal and axillary lymph
464 nodes were studied via flow cytometry or confocal microscopy. Steady state analysis is shown as 4-6
465 mice, representative of at least 3 independent experiments.

466

467 **Immunizations**

468 *In vivo* immunisations were performed with an emulsion Incomplete Freund's Adjuvant (IFA)
469 containing SIINFENKL (OVA) (Hooke Laboratories). Mice were injected with 100 μl of the emulsion
470 subcutaneously, 100 μg OVA per mouse, on the right flank at the height of the hip 7 days after
471 receiving the final administration of tamoxifen. Animals were sacrificed at 5 and 9 days after
472 immunisations and paired analysis of the inguinal and axillary lymph nodes was performed via flow
473 cytometry and confocal microscopy respectively. For B cell responses animals were sacrificed 28 days
474 post-immunisation and serum and lymph nodes were collected. All *in vivo* data immunisation
475 experiments 3-5 mice were used per experiment and data is pooled or representative of 3
476 independent experiments.

477

478 **Flow cytometry**

479 Lymph node single cell suspension of $2.5x10^6$ cells was incubated for 20 min at 4^oC with a purified rat
480 IgG2b anti-mouse CD16/CD32 receptor antibody (BD Biosciences). For stromal cells and lymphocyte
481 staining cells were stained fluorochrome-conjugated antibodies against CD45, CD31, PDPN, CD8a,
482 CD3, CD19, CD4; for innate cell analysis cells were stained for CD11b, B220, CD11c, Ly6C, Ly6G, MerTK,

483 CX3CR1, F4/80, CD169, I-A/I-E, CD207, CD8a, CD64 and CD103 for 25 min at 4°C in PBS containing 1%
484 BSA, 5 mM EDTA, 0.05% NaN3. Cells were incubated with fixable viability stain for 30 min at 4°C.
485 Samples were analysed on BD LSRFortessa x-50 (FACS Symphony) equipped with 100-mW 405-nm,
486 100-mW 488-nm, 150-mW 561-nm, 100-mW 637-nm and 60-mW 355-nm lasers with a ND1.0 filter in
487 front of the FSC photodiode. Data was collected on the FACSDiva software (version 7).
488
489 **Flow cytometry analysis**
490 Flow cytometry data was analysed using FlowJo Software (Tree Star). For tSNE analysis of innate cells,
491 samples were prepared by concatenating approximately 18,000 cells of $CD11b^+$ cells per experimental
492 model. tSNE analysis was performed using the FlowJo package and selected parameters: CD11c,
493 CD103, Ly6c, CD64, CD103, CD8a, F4/80, CD169, MerTK, CX3CR1, MHC class II and CD207. The tSNE
494 package settings were set as: Iterations 1000, perplexity 30, learning rate: 1266; KNN algorithm: Exact;
495 gradient algorithm: Barnes-Hut. Cell groups were defined by the expression of the functional markers
496 used for tSNE analysis.
497
498 **Immunofluorescence of tissue sections**
499 Lymph nodes placed in Antigen fix (DiaPath) and incubated for 2 hours on ice with gentle agitation.
500 Lymph nodes were washed with ice cold PBS and placed in 30% w/v sucrose containing 0.5% NaN3
501 and incubated at 4°C overnight. The LNs were placed into Tissue-Tek optimum cutting temperature
502 compound and then embedded into moulds containing the optimum cutting temperature compound.
503 Samples were sectioned on the Leica cryostat (CM1950) at a thickness of 15 μm.
504
505 For immunofluorescence tissue sections were permeabilised and blocked for 2 hours at room
506 temperature with 10% normal goat serum (NGS), 0.3% Triton X-100in PBS. Primary antibodies were
507 prepared in the dilutions described in Supplementary Table 3 in PBS containing 10% normal goat
508 serum and 0.01% Triton X-1000 and then centrifuged at 15,000g for 5 minutes. The antibody cocktail
509 was added to the tissue sections which were incubated overnight at 4°C. Sections were then incubated
510 at room temperature for 1 hour before being washed with PBS-0.05% Tween 20 (3 x 15 minutes at
511 room temperature). Secondary antibodies were prepared similarly to the primary antibodies and
512 added to the tissue for 2 hours at room temperature. Sections were then washed with PBS-0.05%
513 Tween 20 (2 x 15 minutes), PBS (1 x 10 minutes) and H_2O (1 x 5 minutes) at room temperature and
514 were then mounted using mowiol mounting media. Images of the tissue were obtained on the Leica
515 TCS SP5 with HCX Plan-Apochromat x40 (NA 1.25) oil lenses. Images were captured at 1,024x1,024
516 pixels, three-line and 2-frame average onto hybrid pixel or photomultiplier tube detectors. Imaging

517 areas were manually detected, and z-stacks (15-25 μm) were acquired with intervals at 0.3-0.6 μm.
518 Tile scan boundaries were manually set, and images were stitched automatically (numerical, smooth)
519 using the Leica imaging software (LAS AF-2.7.3.9723). Images were analysed on FiJi software (ImageJ).
520 For analysis of follicles, GCs and the FDC network, tissues sections were blocked and permeabilised
521 with 1% BSA and 2% Triton X-100 for 1hr at room temperature. Sections were stained with IgD-APC,
522 CD21/25-biotin and chicken anti-GFP overnight at 4°C. Sections were washed thrice with PBST 0.05%
523 Tween-20 and incubated with 1ug/mL strepadivin-AF555 and goat anti-chicken-488 (both
524 Thermofisher) for 2hr at 4°C. Sections were washed in PBST and mounted in Hydromount (National
525 Diagnostics) and 40X tile scanned images acquired on a Zeiss LSM-780 at Imperial College London's
526 FILM facility.
527
528 **Image analysis**
529 Lymph node section fibroblast network was analysed in the parenchymal region of lymph nodes using
530 the Mitochondrial Network Analysis (MiNA) toolset (*50*). Quantification was performed on ImageJ
531 using the MiNA 3.0.1 macro available on https://gitgub.com/StuartLab/MiNA. Pre-processing of
532 images was set as follows: median filter radius=5, unsharp mask filter radius=10, mask weight=0.6,
533 CLAHE blocksize=127, histogram bins=256 and max slope=3. Data output from MiNA 3.0.1 quantified
534 the mean branch length as the mean length of all lines used to represent the fibroblastic network
535 structures; mean number of network branches the mean number of attached lines used to represent
536 each structure; and the network footprint as the area or volume of the image consumed by the
537 network signal. To quantify $CD11b^+$ cell number and circularity index in the lymph node parenchyma,
538 uniformly sized maximum projections were acquired and processed in Fiji (ImageJ) with smoothing,
539 Gaussian blur (radius =2), and Otsu thresholding. The 'Fill Holes' and 'Watershed' functions were then
540 applied, and particles between 20-100um^2 were analysed for cell count and circularity. For analysis
541 of B follicles and GCs, antibody staining was thresholded and masked using a custom ImageJ macro to
542 define individual B cell follicles (IgD) and the FDC network (CD21/35). GCs were manually defined as
543 IgD-negative within IgD^+ follicles and containing FDCs. The follicle and GC area and size of the
544 corresponding FDC network were determined using the measurement tool (ImageJ). Image analysis
545 was performed on at least 4 different lymph nodes from independent experiments.
546
547 **Serum ELISAs**
548 ELISA plates were coated with 50 μl/well of Ovalbumin at 100 μg/ml or PBS and incubated at 4°C
549 overnight. Plates were washed twice with PBS-Tween and then blocked for 2 hours at room
550 temperature on a shaker with 100 ml/well with PBS containing 5% powdered milk. After washing twice

551 with PBS-Tween, 2-fold dilutions of serum were prepared in blocking buffer at a starting dilution of
552 1:10, adding 100 μl/well for 2 hours at room temperature on a shaker. Wells were washed three times
553 with PBS-Tween and 50 μl/well of biotinylated detection antibody was added (0.5 μg/ml in 1% BSA)
554 for 1.5 hours at temperature on a shaker. Antibodies IgG1 (BD553441, clone – A85-1), IgG2a
555 (BD553388, clone – R19-15) and IgE (BD553419, clone – R35-118). Plates were washed 5 times with
556 PBS-Tween and 50 μl/well of Streptavidin-HRP (Sigma) was added for 30 minutes at room temperature
557 in the dark. After washing 3 times with PBS-Tween, 100 μl/well of TMB substrate (Life Technologies)
558 followed by 50 μl/well of 1M H2SO4 (stop substrate) were added. Optical density was read at 405 nm
559 on a SpectraMax Plus plate reader.
560
561 **Western Blotting**
562 Control FRCs or shRNA knockdown (PDPN-KD) cells were previously described by Acton et al. 2014(*6*).
563 Cells were grown to ~90% confluency in 145 mm plates and washed in ice-cold 1X tris-buffered saline
564 pH 7.4 (TBS), scraped from dishes on ice and collected in micro-centrifuge tubes in 2 ml of ice-cold
565 TBS. After 10 second table-top centrifugation, supernatants were removed, and cell pellets were
566 triturated in 600 μl of ice-cold 0.1% NP-40. Protein was quantified using 5X Protein Assay Dye Reagent
567 Concentrate (BioRad, 5000006). 6X Laemmli reducing sample buffer was added to 1X final
568 concentration followed by boiling at 95°C for 10 min. Samples were loaded and electrophoresed using
569 4-20% sodium dodecyl sulphate polyacrylamide gel electrophoresis (SDS-PAGE) and transferred to
570 PVDF membranes for 2 hrs 30 min at 65 V. Membranes were blocked in 2.5% milk and 2.5% BSA in
571 0.1% TBS-Tween (TBS-T), for 1hr at room temperature. Membranes were incubated with antibodies
572 in 0.5% milk and 0.5% BSA in 0.1% TBS-T at 4°C overnight. Membranes were washed with 0.1% TBS-T
573 followed by incubation for 2hrs with HRP-conjugated secondary antibodies in 0.5% milk and 0.5% BSA
574 in 0.1% TBS-T. After washing with TBS-T, target protein signals were detected by ECL (GE Healthcare)
575 and visualised using an ImageQuant (GE Lifesciences).
576
577 **Bulk RNA-seq and reads processing**
578 RNA sequencing data from Martinez et al., 2019 are publicly available through University College
579 London's research data repository (doi:10.5522/04/c.4696979). Differential expression analysis was
580 performed using R 4.0.5 and the DESeq2 package. The gene raw count table (*34*) was used to calculate
581 differences in transcript expression between samples. As recommended in the package
582 documentation, transcripts with fewer than 10 counts in total were removed from differential
583 expression analysis. In all, 21285 genes were kept after prefiltering. DESeq2 was used to calculate
584 differences in transcript expression in either PDPN-WT vs PDPN-KO samples, PDPN-WT no CLEC-2 vs

585 CLEC-2 at 6 hours, or PDPN-WT no CLEC-2 vs CLEC-2 at 24 hours (using the contrast function).
586 Differentially expressed genes for each comparison were defined as those with an adjusted p-value
587 smaller than 0.05 and a fold change log2FC<1.6. (downregulated) or log_2FC >1.6 (upregulated). The
588 dplyr package was used for filtering the genes according to their adjusted p-values and fold change.
589 Venn diagrams were plotted using the VennDiagram package. Heatmaps were plotted using TPM
590 (transcript per million) values normalised per gene (Z-score) and clustered using hierarchical clustering
591 using the pheatmap and hclust R packages. Colour palettes were generated using the RColorBrewer
592 package. DAVID (*67*) was for functional annotation. The list of differentially expressed genes (using
593 official gene symbols) was uploaded to the DAVID website (https://david.ncifcrf.gov/summary.jsp).
594 The table output was then processed using a custom R script. The terms were filtered by fold discovery
595 rate (FDR≤0.05), sorted by fold enrichment and plotted using the dplyr and ggplot2 packages. The
596 annotated GO terms were used to identify the transcription factors in the list. Genes were mapped to
597 GO terms using the biomaRt package for R. Transcription factors were then filtered as genes mapped
598 with the GO:0003700 (DNA-binding transcription factor activity) term. Fold change values were
599 plotted using the ggdotchart package. Functional network analysis was carried out using STRING. The
600 lists of differentially expressed genes were submitted to the STRING website (string-db.org/) and
601 analysed using the default values except for the confidence threshold and retaining physical and
602 functional interactions. The confidence threshold was set to the most restrictive value ("very high",
603 0.9). The networks were then analysed in Cytoscape (*68*) for visualisation and clustering. Nodes that
604 did not form part of a larger network were hidden (retaining nodes with at least 3 neighbours at level
605 3). Clustering was performed with the MCODE algorithm (*69*) using the default parameters. Clusters
606 were manually labelled based on the annotated gene names and descriptions. We filtered the GO
607 terms by statistical relevance and sorted them by fold enrichment (mapped/expected).
608
609 **scRNA-seq analysis**
610 Inguinal, axillary and brachial lymph nodes were collected from PDGFRα^{mGFP} (Control) and
611 PDGFR$\alpha^{mGFP\Delta PDPN}$ mice (6 mice per group) and an identical number of cells was pooled from each
612 replicate. Cells were separated by autoMACS (following manufacturers protocol) sorting into two
613 groups: $CD45^-CD31^-$ and $CD45^+CD31^+$. Purity check of the enriched cells was performed by flow
614 cytometry. Cells were divided into 4 groups: Control_$CD45^-CD31^-$, ΔPDPN_$CD45^-CD31^-$,
615 Control_$CD45^+CD31^+$ and ΔPDPN_$CD45^+CD31^+$. Cells were processed through the Chromium Single-
616 Cell 3' v2 Library Kit (10x Genomics) at QMUL, Genome Centre. After quality control, 12825 $CD45^-$
617 $CD31^-$ cells (fibroblasts) from the Control mice (median genes/cell= 3213, median reads/cell = 43452)
618 and 10246 $CD45^-CD31^-$ cells (fibroblasts) from the ΔPDPN mice (Median genes/cell=3567, median

619 reads/cell = 43452) were analysed. For $CD45^+CD31^+$ enriched cells, after quality control, 6212 $CD45^+$
620 and $CD31^+$ cells from the PDGFRα^{mGFP} (Control) mice (median genes/cell= 2227, median reads/cell =
621 49746) and PDGFR$\alpha^{mGFP\Delta PDPN}$ (ΔPDPN) mice (Median genes/cell=2439, median reads/cell = 42869)
622 were analysed. All scRNA-seq analysis for datasets, and subcluster analysis, was performed using the
623 filtering, normalisation and marker identification codes previously published by Seurat et al. using
624 Seurat (*70–74*). Clustering of cells was performed on merged datasets of PDGFRα^{mGFP} (Control) and
625 PDGFR$\alpha^{mGFP\Delta PDPN}$ (ΔPDPN) cells. For cell communication stromal cells were set as the sources and
626 immune cells as the targets. *Milo* was utilised to measured ifferential abundance analysis on KNN
627 graphs (miloR) (*41*). Pseudotime trajectory analysis was performed on UMAP embedding using
628 Monocle 3 v.1.0.0 package and the *Cd34*$^+$ SC subcluster expressing *Pi16* neighbourhood was selected
629 as the root (*75*). For analysis combining both $CD45^-CD31^-$ and $CD45^+CD31^+$ datasets, 6212 per
630 condition were down-sampled and merged before analysis (Seurat code). Cell-cell communication
631 between stromal and immune cells in PDGFRα^{mGFP} (Control) and PDGFR$\alpha^{mGFP\Delta PDPN}$ was measured using
632 CellChat (*55*, *56*). No new codes were developed to perform analysis in this manuscript.
633
634 **Prism and statistics**
635 Prism9 Software (GraphPad) was used to create graphs and statistical analysis. Comparisons of two
636 data sets was performed using two-tailed Mann-Whitney tests. For serum ELISA the Wilcoxon test was
637 used and p-values are indicated. For comparisons of multiple groups was performed using one- or
638 two-way ANOVA with Tukey's multiple comparison. For all tests, $p<0.05$ was considered significant
639
640 **Supplementary Materials**
641 Fig. S1 to S8
642 Table S1 to S15
643

References and Notes

1. A. L. Fletcher, S. E. Acton, K. Knoblich, Lymph node fibroblastic reticular cells in health and disease. *Nature Publishing Group* **15**, 1–12 (2015).

2. A. T. Krishnamurty, S. J. Turley, Lymph node stromal cells: cartographers of the immune system. *Nature Immunology* **21**, 1–12 (2020).

3. S. E. Acton, L. Onder, M. Novkovic, V. G. Martinez, B. Ludewig, Communication, construction, and fluid control: lymphoid organ fibroblastic reticular cell and conduit networks. *Trends Immunol* **42**, 782–794 (2021).

4. M. Simic, I. Manosalva, L. Spinelli, R. Gentek, R. R. Shayan, C. Siret, M. Girard-Madoux, S. Wang, L. de Fabritus, J. Verschoor, Y. M. Kerdiles, M. Bajénoff, R. Stumm, R. Golub, S. A. van de Pavert, Distinct Waves from the Hemogenic Endothelium Give Rise to Layered Lymphoid Tissue Inducer Cell Ontogeny. *CellReports* **32**, 108004 (2020).

5. S. Makris, C. M. de Winde, H. L. Horsnell, J. A. Cantoral-Rebordinos, R. E. Finlay, S. E. Acton, Immune function and dysfunction are determined by lymphoid tissue efficacy. *Dis Model Mech* **15**, dmm049256 (2022).

6. S. E. Acton, A. J. Farrugia, J. L. Astarita, D. Mourão-Sá, R. P. Jenkins, E. Nye, S. Hooper, J. van Blijswijk, N. C. Rogers, K. J. Snelgrove, I. Rosewell, L. F. Moita, G. Stamp, S. J. Turley, E. Sahai, C. R. e Sousa, Dendritic cells control fibroblastic reticular network tension and lymph node expansion. *Nature Publishing Group* **514**, 498–502 (2014).

7. J. L. Astarita, V. Cremasco, J. Fu, M. C. Darnell, J. R. Peck, J. M. Nieves-Bonilla, K. Song, Y. Kondo, M. C. Woodruff, A. Gogineni, L. Onder, B. Ludewig, R. M. Weimer, M. C. Carroll, D. J. Mooney, L. Xia, S. J. Turley, The CLEC-2–podoplanin axis controls the contractility of fibroblastic reticular cells and lymph node microarchitecture. *Nat Immunol* **16**, 75–84 (2015).

8. H. L. Horsnell, R. J. Tetley, H. D. Belly, S. Makris, L. J. Millward, A. C. Benjamin, L. A. Heeringa, C. M. de Winde, E. K. Paluch, Y. Mao, S. E. Acton, Lymph node homeostasis and adaptation to immune challenge resolved by fibroblast network mechanics. *Nat Immunol* **23**, 1169–1182 (2022).

9. M. B. Buechler, R. N. Pradhan, A. T. Krishnamurty, C. Cox, A. K. Calviello, A. W. Wang, Y. A. Yang, L. Tam, R. Caothien, M. Roose-Girma, Z. Modrusan, J. R. Arron, R. Bourgon, S. Müller, S. J. Turley, Cross-tissue organization of the fibroblast lineage. *Nature* **593**, 575–579 (2021).

10. S. Y. Choi, H. Bae, S.-H. Jeong, I. Park, H. Cho, S. P. Hong, D.-H. Lee, C. Lee, J.-S. Park, S. H. Suh, J. Choi, M. J. Yang, J. Y. Jang, L. Onder, J. H. Moon, H.-S. Jeong, R. H. Adams, J.-M. Kim, B. Ludewig, J.-H. Song, D.-S. Lim, G. Y. Koh, YAP/TAZ direct commitment and maturation of lymph node fibroblastic reticular cells. *Nature Communications* **11**, 519–15 (2020).

11. A. E. Denton, E. J. Carr, L. P. Magiera, A. J. B. Watts, D. T. Fearon, Embryonic FAP+ lymphoid tissue organizer cells generate the reticular network of adult lymph nodes. *J. Exp. Med.* **216**, 2242–2252 (2019).

12. I. Cinti, A. E. Denton, Lymphoid stromal cells—more than just a highway to humoral immunity. *Oxf Open Immunol* **2**, iqab011 (2021).

13. L. B. Rodda, E. Lu, M. L. Bennett, C. L. Sokol, X. Wang, S. A. Luther, B. A. Barres, A. D. Luster, C. J. Ye, J. G. Cyster, Single-Cell RNA Sequencing of Lymph Node Stromal Cells Reveals Niche-Associated Heterogeneity. *Immunity* **48**, 1014-1028.e6 (2018).

14. M. H. Ulvmar, K. Werth, A. Braun, P. Kelay, E. Hub, K. Eller, L. Chan, B. Lucas, I. Novitzky-Basso, K. Nakamura, T. Rülicke, R. J. B. Nibbs, T. Worbs, R. Förster, A. Rot, The atypical chemokine receptor CCRL1 shapes functional CCL21 gradients in lymph nodes. *Nature Immunology* **15**, 623–630 (2014).

15. L. Menzel, M. Zschummel, T. Crowley, V. Franke, M. Grau, C. Ulbricht, A. Hauser, V. Siffrin, M. Bajénoff, S. E. Acton, A. Akalin, G. Lenz, G. Willimsky, U. E. Höpken, A. Rehm, Lymphocyte access to lymphoma is impaired by high endothelial venule regression. *Cell Reports* **37**, 109878 (2021).

16. R. T. Boscacci, F. Pfeiffer, K. Gollmer, A. I. C. Sevilla, A. M. Martin, S. F. Soriano, D. Natale, S. Henrickson, U. H. von Andrian, Y. Fukui, M. Mellado, U. Deutsch, B. Engelhardt, J. V. Stein, Comprehensive analysis of lymph node stroma-expressed Ig superfamily members reveals redundant and nonredundant roles for ICAM-1, ICAM-2, and VCAM-1 in lymphocyte homing. *Blood* **116**, 915–925 (2010).

17. V. Cremasco, M. C. Woodruff, L. Onder, J. Cupovic, J. M. Nieves-Bonilla, F. A. Schildberg, J. Chang, F. Cremasco, C. J. Harvey, K. Wucherpfennig, B. Ludewig, M. C. Carroll, S. J. Turley, B cell homeostasis and follicle confines are governed by fibroblastic reticular cells. *Nature Immunology* **15**, 973–981 (2014).

18. H.-Y. Huang, A. Rivas-Caicedo, F. Renevey, H. Cannelle, E. Peranzoni, L. Scarpellino, D. L. Hardie, A. Pommier, K. Schaeuble, S. Favre, T. K. Vogt, F. Arenzana-Seisdedos, P. Schneider, C. D. Buckley, E. Donnadieu, S. A. Luther, Identification of a new subset of lymph node stromal cells involved in regulating plasma cell homeostasis. *Proc. Natl. Acad. Sci. U.S.A.* **115**, E6826–E6835 (2018).

19. C. Mionnet, I. Mondor, A. Jorquera, M. Loosveld, J. Maurizio, M.-L. Arcangeli, N. H. Ruddle, J. Nowak, M. Aurrand-Lions, H. Luche, M. Bajénoff, Identification of a New Stromal Cell Type Involved in the Regulation of Inflamed B Cell Follicles. *PLoS Biol* **11**, e1001672-13 (2013).

20. M. Quintanilla, L. Montero-Montero, J. Renart, E. Martín-Villar, Podoplanin in Inflammation and Cancer. *Int J Mol Sci* **20**, 707 (2019).

21. J. L. Astarita, S. E. Acton, S. J. Turley, Podoplanin: emerging functions in development, the immune system, and cancer. *Front Immunol* **3**, 283 (2012).

22. K. Matsui, S. Breiteneder-Geleff, D. Kerjaschki, Epitope-specific antibodies to the 43-kD glomerular membrane protein podoplanin cause proteinuria and rapid flattening of podocytes. *J Am Soc Nephrol* **9**, 2013–2026 (1998).

23. A. Wetterwald, W. Hofstetter, M. G. Cecchini, B. Lanske, C. Wagner, H. Fleisch, M. Atkinson, Characterization and cloning of the E11 antigen, a marker expressed by Rat Osteoblasts and Osteocytes. *Bone* **18**, 125–132 (1996).

24. A. K. Rishi, M. Joyce-Brady, J. Fisher, L. G. Dobbs, J. Floros, J. VanderSpek, J. S. Brody, M. C. Williams, Cloning, Characterization, and Developmental Expression of a Rat Lung Alveolar Type I Cell Gene in Embryonic Endodermal and Neural Derivatives. *Dev Biol* **167**, 294–306 (1995).

25. F. G. Scholl, C. Gamallo, S. Vilar?o, M. Quintanilla, Identification of PA2.26 antigen as a novel cell-surface mucin-type glycoprotein that induces plasma membrane extensions and increased motility in keratinocytes. *J Cell Sci* **112**, 4601–4613 (1999).

26. S. Jalkanen, M. Salmi, Lymphatic endothelial cells of the lymph node. *Nat Rev Immunol* **20**, 566–578 (2020).

27. S. E. Acton, J. L. Astarita, D. Malhotra, V. Lukacs-Kornek, B. Franz, P. R. Hess, Z. Jakus, M. Kuligowski, A. L. Fletcher, K. G. Elpek, A. Bellemare-Pelletier, L. Sceats, E. D. Reynoso, S. F. Gonzalez, D. B. Graham, J. Chang, A. Peters, M. Woodruff, Y.-A. Kim, W. Swat, T. Morita, V. Kuchroo, M. C. Carroll, M. L. Kahn, K. W. Wucherpfennig, S. J. Turley, Podoplanin-Rich Stromal Networks Induce Dendritic Cell Motility via Activation of the C-type Lectin Receptor CLEC-2. *Immunity* **37**, 276–289 (2012).

28. A. Link, T. K. Vogt, S. Favre, M. R. Britschgi, H. Acha-Orbea, B. Hinz, J. G. Cyster, S. A. Luther, Fibroblastic reticular cells in lymph nodes regulate the homeostasis of naive T cells. *Nature Immunology* **8**, 1255–1265 (2007).

29. D. O. Dias, H. Kim, D. Holl, B. W. Solnestam, J. Lundeberg, M. Carlén, C. Göritz, J. Frisén, Reducing Pericyte-Derived Scarring Promotes Recovery after Spinal Cord Injury. *Cell* **173**, 153-165.e22 (2018).

30. M. J. D. Rey, R. Faré, E. Izquierdo, A. Usategui, J. L. Rodríguez-Fernández, A. Suárez-Fueyo, J. D. Cañete, J. L. Pablos, Clinicopathological Correlations of Podoplanin (gp38) Expression in Rheumatoid Synovium and Its Potential Contribution to Fibroblast Platelet Crosstalk. *Plos One* **9**, e99607 (2014).

31. H. Krishnan, J. Rayes, T. Miyashita, G. Ishii, E. P. Retzbach, S. A. Sheehan, A. Takemoto, Y. Chang, K. Yoneda, J. Asai, L. Jensen, L. Chalise, A. Natsume, G. S. Goldberg, Podoplanin: An emerging cancer biomarker and therapeutic target. *Cancer Sci* **109**, 1292–1299 (2018).

32. M. Nurmik, P. Ullmann, F. Rodriguez, S. Haan, E. Letellier, In search of definitions: Cancer-associated fibroblasts and their markers. *Int J Cancer* **146**, 895–905 (2020).

33. L. S. C. Ward, L. Sheriff, J. L. Marshall, J. E. Manning, A. Brill, G. B. Nash, H. M. McGettrick, Podoplanin regulates the migration of mesenchymal stromal cells and their interaction with platelets. *J Cell Sci* **132**, jcs222067 (2019).

34. V. G. Martinez, V. Pankova, L. Krasny, T. Singh, S. Makris, I. J. White, A. C. Benjamin, S. Dertschnig, H. L. Horsnell, J. Kriston-Vizi, J. J. Burden, P. H. Huang, C. J. Tape, S. E. Acton, Fibroblastic Reticular Cells Control Conduit Matrix Deposition during Lymph Node Expansion. *CellReports* **29**, 2810-2822.e5 (2019).

35. E. Martín-Villar, D. Megías, S. Castel, M. M. Yurrita, S. Vilaró, M. Quintanilla, Podoplanin binds ERM proteins to activate RhoA and promote epithelial-mesenchymal transition. *J Cell Sci* **119**, 4541–4553 (2006).

36. A. García-Ortiz, J. M. Serrador, ERM Proteins at the Crossroad of Leukocyte Polarization, Migration and Intercellular Adhesion. *Int J Mol Sci* **21**, 1502 (2020).

37. A. Peters, L. A. Pitcher, J. M. Sullivan, M. Mitsdoerffer, S. E. Acton, B. Franz, K. Wucherpfennig, S. Turley, M. C. Carroll, R. A. Sobel, E. Bettelli, V. K. Kuchroo, Th17 Cells Induce Ectopic Lymphoid Follicles in Central Nervous System Tissue Inflammation. *Immunity* **35**, 986–996 (2011).

38. P. Uhrin, J. Zaujec, J. M. Breuss, D. Olcaydu, P. Chrenek, H. Stockinger, E. Fuertbauer, M. Moser, P. Haiko, R. Fässler, K. Alitalo, B. R. Binder, D. Kerjaschki, Novel function for blood platelets and podoplanin in developmental separation of blood and lymphatic circulation. *Blood* **115**, 3997–4005 (2010).

39. C. Bénézech, S. Nayar, B. A. Finney, D. R. Withers, K. Lowe, G. E. Desanti, C. L. Marriott, S. P. Watson, J. H. Caamaño, C. D. Buckley, F. Barone, CLEC-2 is required for development and maintenance of lymph nodes. *Blood* **123**, 3200–3207 (2014).

40. D. Malhotra, J. Astarita, V. Lukacs-Kornek, P. Tayalia, S. F. Gonzalez, S. K. Chang, K. Knoblich, M. E. Hemler, M. B. Brenner, M. C. Carroll, D. J. Mooney, S. J. Turley, the I. G. P. Consortium, Y. Zhou, S. A. Shinton, R. R. Hardy, N. A. Bezman, J. C. Sun, C. C. Kim, L. L. Lanier, J. Miller, B. Brown, M. Merad, A. L. Fletcher, K. G. Elpek, A. Bellemare-Pelletier, K. Narayan, K. Sylvia, J. Kang, R. Gazit, B. Garrison,

D. J. Rossi, V. Jojic, D. Koller, R. Jianu, D. Laidlaw, J. Costello, J. Collins, N. Cohen, P. Brennan, M. B. Brenner, T. Shay, A. Regev, F. Kim, T. N. Rao, A. Wagers, E. L. Gautier, C. Jakubzick, G. J. Randolph, P. Monach, A. J. Best, J. Knell, A. Goldrath, T. Heng, T. Kreslavsky, M. Painter, D. Mathis, C. Benoist, Transcriptional profiling of stroma from inflamed and resting lymph nodes defines immunological hallmarks. *Nature Immunology* **13**, 499 (2012).

41. E. Dann, N. C. Henderson, S. A. Teichmann, M. D. Morgan, J. C. Marioni, Differential abundance testing on single-cell data using k-nearest neighbor graphs. *Nat. Biotechnol.* **40**, 245–253 (2022).

42. M. B. Buechler, W. Fu, S. J. Turley, Fibroblast-macrophage reciprocal interactions in health, fibrosis, and cancer. *Immunity* **54**, 903–915 (2021).

43. S. Pestka, C. D. Krause, M. R. Walter, Interferons, interferon-like cytokines, and their receptors. *Immunological Reviews* **202**, 8–32 (2004).

44. K. M. Sitnik, K. Wendland, H. Weishaupt, H. Uronen-Hansson, A. J. White, G. Anderson, K. Kotarsky, W. W. Agace, Context-Dependent Development of Lymphoid Stroma from Adult CD34+ Adventitial Progenitors. *Cell Rep.* **14**, 2375–2388 (2016).

45. S. Bhattacharyya, W. Wang, L. Morales-Nebreda, G. Feng, M. Wu, X. Zhou, R. Lafyatis, J. Lee, M. Hinchcliff, C. Feghali-Bostwick, K. Lakota, G. R. S. Budinger, K. Raparia, Z. Tamaki, J. Varga, Tenascin-C drives persistence of organ fibrosis. *Nat. Commun.* **7**, 11703 (2016).

46. D. Katoh, Y. Kozuka, A. Noro, T. Ogawa, K. Imanaka-Yoshida, T. Yoshida, Tenascin-C Induces Phenotypic Changes in Fibroblasts to Myofibroblasts with High Contractility through the Integrin αvβ1/Transforming Growth Factor β/SMAD Signaling Axis in Human Breast Cancer. *Am. J. Pathol.* **190**, 2123–2135 (2020).

47. C. Bénézech, E. Mader, G. Desanti, M. Khan, K. Nakamura, A. White, C. F. Ware, G. Anderson, J. H. Caamaño, Lymphotoxin-β Receptor Signaling through NF-κB2-RelB Pathway Reprograms Adipocyte Precursors as Lymph Node Stromal Cells. *Immunity* **37**, 721–734 (2012).

48. S. Zelenay, A. G. van der Veen, J. P. Böttcher, K. J. Snelgrove, N. Rogers, S. E. Acton, P. Chakravarty, M. R. Girotti, R. Marais, S. A. Quezada, E. Sahai, C. Reis e Sousa, Cyclooxygenase-Dependent Tumor Growth through Evasion of Immunity. *Cell* **162**, 1257–1270 (2015).

49. M. Yu, G. Guo, X. Zhang, L. Li, W. Yang, R. Bollag, Y. Cui, Fibroblastic reticular cells of the lymphoid tissues modulate T cell activation threshold during homeostasis via hyperactive cyclooxygenase-2/prostaglandin E2 axis. *Sci. Rep.* **7**, 3350 (2017).

50. A. J. Valente, L. A. Maddalena, E. L. Robb, F. Moradi, J. A. Stuart, A simple ImageJ macro tool for analyzing mitochondrial network morphology in mammalian cell culture. *Acta Histochem* **119**, 315–326 (2017).

51. L. Fang, Y. Che, C. Zhang, J. Huang, Y. Lei, Z. Lu, N. Sun, J. He, PLAU directs conversion of fibroblasts to inflammatory cancer-associated fibroblasts, promoting esophageal squamous cell carcinoma progression via uPAR/Akt/NF-κB/IL8 pathway. *Cell Death Discov.* **7**, 32 (2021).

52. J.-M. Li, D. C. Yang, J. Oldham, A. Linderholm, J. Zhang, J. Liu, N. J. Kenyon, C.-H. Chen, Therapeutic targeting of argininosuccinate synthase 1 (ASS1)-deficient pulmonary fibrosis. *Mol. Ther.* **29**, 1487–1500 (2021).

53. S. E. Lim, M. D. Joseph, C. M. de Winde, S. E. Acton, S. Simoncelli, Quantitative single molecule analysis of podoplanin clustering in fibroblastic reticular cells uncovers CD44 function. *Open Biol.* **13**, 220377 (2023).

54. B. H. Herzog, J. Fu, S. J. Wilson, P. R. Hess, A. Sen, J. M. McDaniel, Y. Pan, M. Sheng, T. Yago, R. Silasi-Mansat, S. McGee, F. May, B. Nieswandt, A. J. Morris, F. Lupu, S. R. Coughlin, R. P. McEver, H. Chen, M. L. Kahn, L. Xia, Podoplanin maintains high endothelial venule integrity by interacting with platelet CLEC-2. *Nature* **502**, 105–109 (2013).

55. S. Jin, M. V. Plikus, Q. Nie, CellChat for systematic analysis of cell-cell communication from single-cell and spatially resolved transcriptomics. *bioRxiv*, 2023.11.05.565674 (2023).

56. S. Jin, C. F. Guerrero-Juarez, L. Zhang, I. Chang, R. Ramos, C.-H. Kuan, P. Myung, M. V. Plikus, Q. Nie, Inference and analysis of cell-cell communication using CellChat. *Nat. Commun.* **12**, 1088 (2021).

57. K. Rawat, A. Tewari, X. Li, A. B. Mara, W. T. King, S. L. Gibbings, C. F. Nnam, F. W. Kolling, B. N. Lambrecht, C. V. Jakubzick, CCL5-producing migratory dendritic cells guide CCR5+ monocytes into the draining lymph nodes. *J. Exp. Med.* **220**, e20222129 (2023).

58. J. G. Cyster, B cell follicles and antigen encounters of the third kind. *Nat Immunol* **11**, 989–996 (2010).

59. B. Poligone, A. S. Baldwin, Positive and Negative Regulation of NF-κB by COX-2 ROLES OF DIFFERENT PROSTAGLANDINS*. *J. Biol. Chem.* **276**, 38658–38664 (2001).

60. M. P. Charalambous, T. Lightfoot, V. Speirs, K. Horgan, N. J. Gooderham, Expression of COX-2, NF-κB-p65, NF-κB-p50 and IKKα in malignant and adjacent normal human colorectal tissue. *Br. J. Cancer* **101**, 106–115 (2009).

61. A. E. Denton, J. Dooley, I. Cinti, A. Silva-Cayetano, S. Fra-Bido, S. Innocentin, D. L. Hill, E. J. Carr, A. N. J. McKenzie, A. Liston, M. A. Linterman, Targeting TLR4 during vaccination boosts MAdCAM-1+ lymphoid stromal cell activation and promotes the aged germinal center response. *Sci. Immunol.* **7**, eabk0018 (2022).

62. S. Nayar, J. Campos, C. G. Smith, V. Iannizzotto, D. H. Gardner, F. Mourcin, D. Roulois, J. Turner, M. Sylvestre, S. Asam, B. Glaysher, S. J. Bowman, D. T. Fearon, A. Filer, K. Tarte, S. A. Luther, B. A. Fisher, C. D. Buckley, M. C. Coles, F. Barone, Immunofibroblasts are pivotal drivers of tertiary lymphoid structure formation and local pathology. *Proc. Natl. Acad. Sci.* **116**, 13490–13497 (2019).

63. B. Apollonio, F. Spada, N. Petrov, D. Cozzetto, D. Papazoglou, P. Jarvis, S. Kannambath, M. Terranova-Barberio, R.-M. Amini, G. Enblad, C. E. Graham, R. Benjamin, E. H. Phillips, R. J. Ellis, R. Nuamah, M. Saqi, D. P. Calado, R. Rosenquist, L. A. Sutton, J. R. Salisbury, G. Zacharioudakis, A. Vardi, P. R. Hagner, A. K. Gandhi, M. Bacac, C. Claus, P. Umana, R. F. Jarrett, C. Klein, A. J. A. Deutsch, A. G. Ramsay, Tumor-activated lymph node fibroblasts suppress T cell function in diffuse large B cell lymphoma. *J. Clin. Investig.* **133** (2023).

64. M. D. Lynch, F. M. Watt, Fibroblast heterogeneity: implications for human disease. *J. Clin. Investig.* **128**, 26–35 (2018).

65. S. Davidson, M. Coles, T. Thomas, G. Kollias, B. Ludewig, S. Turley, M. Brenner, C. D. Buckley, Fibroblasts as immune regulators in infection, inflammation and cancer. *Nat Rev Immunol*, 1–14 (2021).

66. E. Sahai, I. Astsaturov, E. Cukierman, D. G. DeNardo, M. Egeblad, R. M. Evans, D. Fearon, F. R. Greten, S. R. Hingorani, T. Hunter, R. O. Hynes, R. K. Jain, T. Janowitz, C. Jorgensen, A. C. Kimmelman, M. G. Kolonin, R. G. Maki, R. S. Powers, E. Puré, D. C. Ramirez, R. Scherz-Shouval, M. H. Sherman, S. Stewart, T. D. Tlsty, D. A. Tuveson, F. M. Watt, V. Weaver, A. T. Weeraratna, Z. Werb, A framework for advancing our understanding of cancer-associated fibroblasts. *Nature Reviews Cancer* **20**, 174–186 (2020).

67. B. T. Sherman, M. Hao, J. Qiu, X. Jiao, M. W. Baseler, H. C. Lane, T. Imamichi, W. Chang, DAVID: a web server for functional enrichment analysis and functional annotation of gene lists (2021 update). *Nucleic Acids Res* **50**, W216–W221 (2022).

68. P. Shannon, A. Markiel, O. Ozier, N. S. Baliga, J. T. Wang, D. Ramage, N. Amin, B. Schwikowski, T. Ideker, Cytoscape: A Software Environment for Integrated Models of Biomolecular Interaction Networks. *Genome Res* **13**, 2498–2504 (2003).

69. G. D. Bader, C. W. Hogue, An automated method for finding molecular complexes in large protein interaction networks. *Bmc Bioinformatics* **4**, 2 (2003).

70. R. Satija, J. A. Farrell, D. Gennert, A. F. Schier, A. Regev, Spatial reconstruction of single-cell gene expression data. *Nat. Biotechnol.* **33**, 495–502 (2015).

71. Y. Hao, T. Stuart, M. H. Kowalski, S. Choudhary, P. Hoffman, A. Hartman, A. Srivastava, G. Molla, S. Madad, C. Fernandez-Granda, R. Satija, Dictionary learning for integrative, multimodal and scalable single-cell analysis. *Nat. Biotechnol.* **42**, 293–304 (2024).

72. A. Butler, P. Hoffman, P. Smibert, E. Papalexi, R. Satija, Integrating single-cell transcriptomic data across different conditions, technologies, and species. *Nat. Biotechnol.* **36**, 411–420 (2018).

73. T. Stuart, A. Butler, P. Hoffman, C. Hafemeister, E. Papalexi, W. M. Mauck, Y. Hao, M. Stoeckius, P. Smibert, R. Satija, Comprehensive Integration of Single-Cell Data. *Cell* **177**, 1888-1902.e21 (2019).

74. Y. Hao, S. Hao, E. Andersen-Nissen, W. M. Mauck, S. Zheng, A. Butler, M. J. Lee, A. J. Wilk, C. Darby, M. Zager, P. Hoffman, M. Stoeckius, E. Papalexi, E. P. Mimitou, J. Jain, A. Srivastava, T. Stuart, L. M. Fleming, B. Yeung, A. J. Rogers, J. M. McElrath, C. A. Blish, R. Gottardo, P. Smibert, R. Satija, Integrated analysis of multimodal single-cell data. *Cell* **184**, 3573-3587.e29 (2021).

75. J. Cao, M. Spielmann, X. Qiu, X. Huang, D. M. Ibrahim, A. J. Hill, F. Zhang, S. Mundlos, L. Christiansen, F. J. Steemers, C. Trapnell, J. Shendure, The single-cell transcriptional landscape of mammalian organogenesis. *Nature* **566**, 496–502 (2019).

Acknowledgements

We thank H. Clevers for supplying R26R-confetti mice and S. Watson and C. Buckley for providing the PDPN$^{fl/fl}$ mouse model. We thank the CRUK Centre for Flow Cytometry TTP at UCL Cancer Institute and their staff for support and instrumentation. We thank the Genome Centre at QMUL for processing through the Chromium Single-Cell3' v2 Library Kit (10x Genomics) and performing initial quality control and preparing gene expression libraries. We also thank Professor Sanjiv Luther and (University of Lausanne), Dr. Nagham Alouche (University of Lausanne) and Dr. Delan N. Alasaadi (UCL, LMCB) for critical discussion of data during manuscript preparation.

Funding

This work has been supported by the European Research Council Starting Grant LNEXPANDS (S.E.A.), Cancer Research UK Careers Development Fellowship CRUK-A19763 (S.E.A.), Rosetrees Trust Foundation PGS22 100023-CD1 (S.E.A.), Cancer Research UK Senior Fellowship CRUK - RCCSCF-May22\100001 (S.E.A.) and MRC Career Development award MR/V009591/1 (AED). The LMCB was supported by Medical Research Council (MC-U12266B).

Author contributions

S.M. and S.E.A. designed the study and wrote the manuscript. S.M. performed all *in vivo* experiments, analysed the majority of experiments and performed all scRNA-seq analysis from *in vivo* experiments. Y.H-G., J.A.C-R., V.G.M., H.L.H. and C.M.d.W. performed *in vitro* bulk-RNA-seq analysis. A.C.B. and S.E.A. designed and validated the PDGFRα-mGFP-CreERT2 mouse model. M.J. performed skeletisation image analysis. D.S. performed image analysis of CD11b cells and N.N. performed western blot analysis. I.C and A.D. performed analysis of B cell follicles and Germinal Centres.

Competing Interests

The authors declare they have no competing interests.

Data and Materials Availability:

Bulk RNA sequencing data from Martinez et al., 2019 are publicly available through University College London's research repository (doi:10.5522/04/c.4696979). scRNA-seq data is available through University College London's research repository (under CC0 license).

Supplementary Materials

Fig. S1 to S8

Table S1 to S15

1

Supplementary Figure

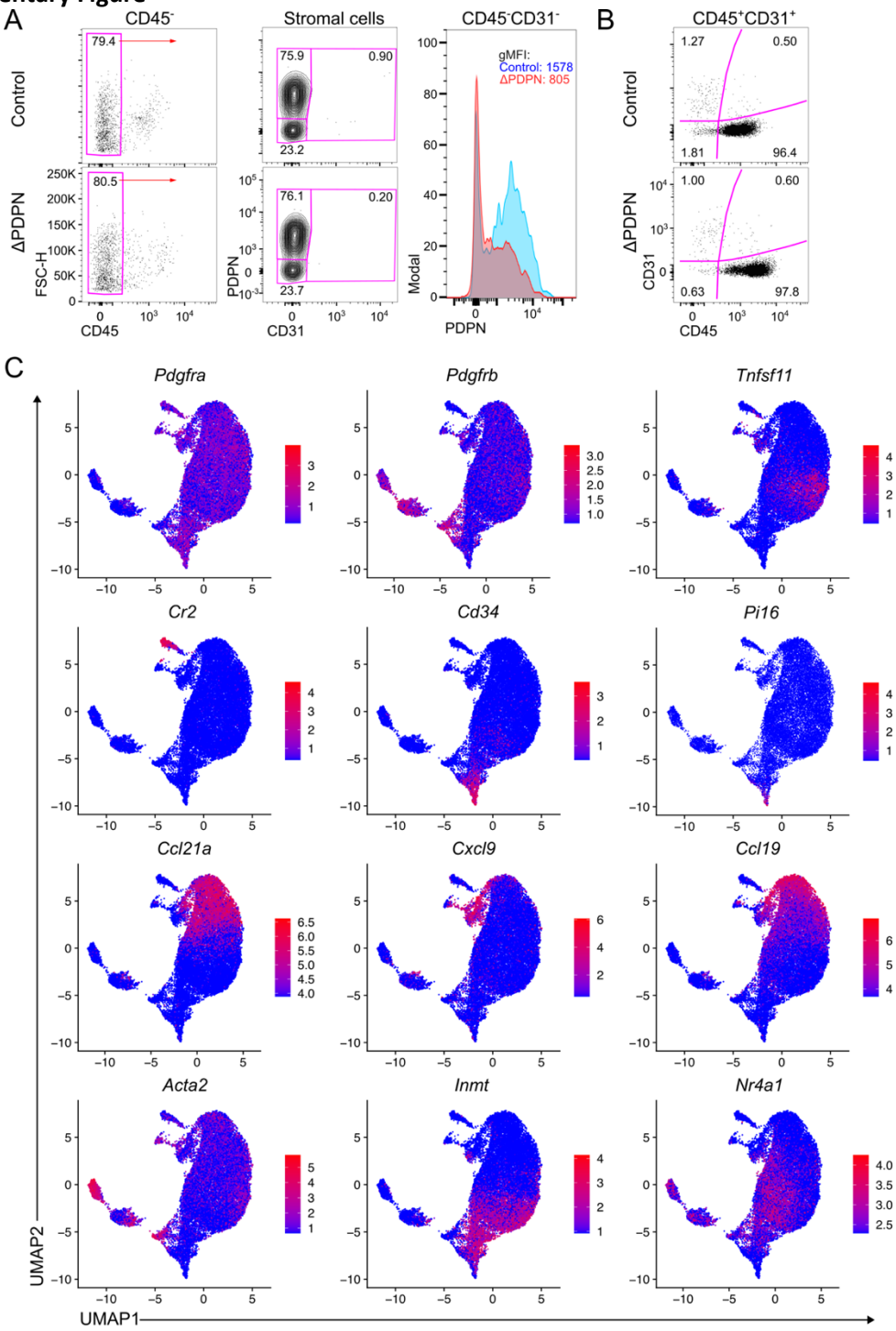

Fig. S1. Cell purity check and gene expression on scRNA-seq analysed stromal cells

(**A**) Enriched stromal cells (CD45⁻CD31⁻) from PDGFRα^{mGFP} (control) or PDGFRα$^{mGFP\Delta PDPN}$ (ΔPDPN) showing purity check (markers: CD45, CD31, PDPN) and histogram of PDPN expression with geometric mean fluorescence intensity (gMFI). (**B**) CD45⁺CD31⁺ (immune and endothelial) enriched cell purity check (markers CD45 and CD31) for PDGFRα^{mGFP} (control) or PDGFRα$^{mGFP\Delta PDPN}$ (ΔPDPN) cells. (**C**) UMAP showing the expression of the primary genes used to define the stromal cell (CD45⁻CD31⁻) clusters.

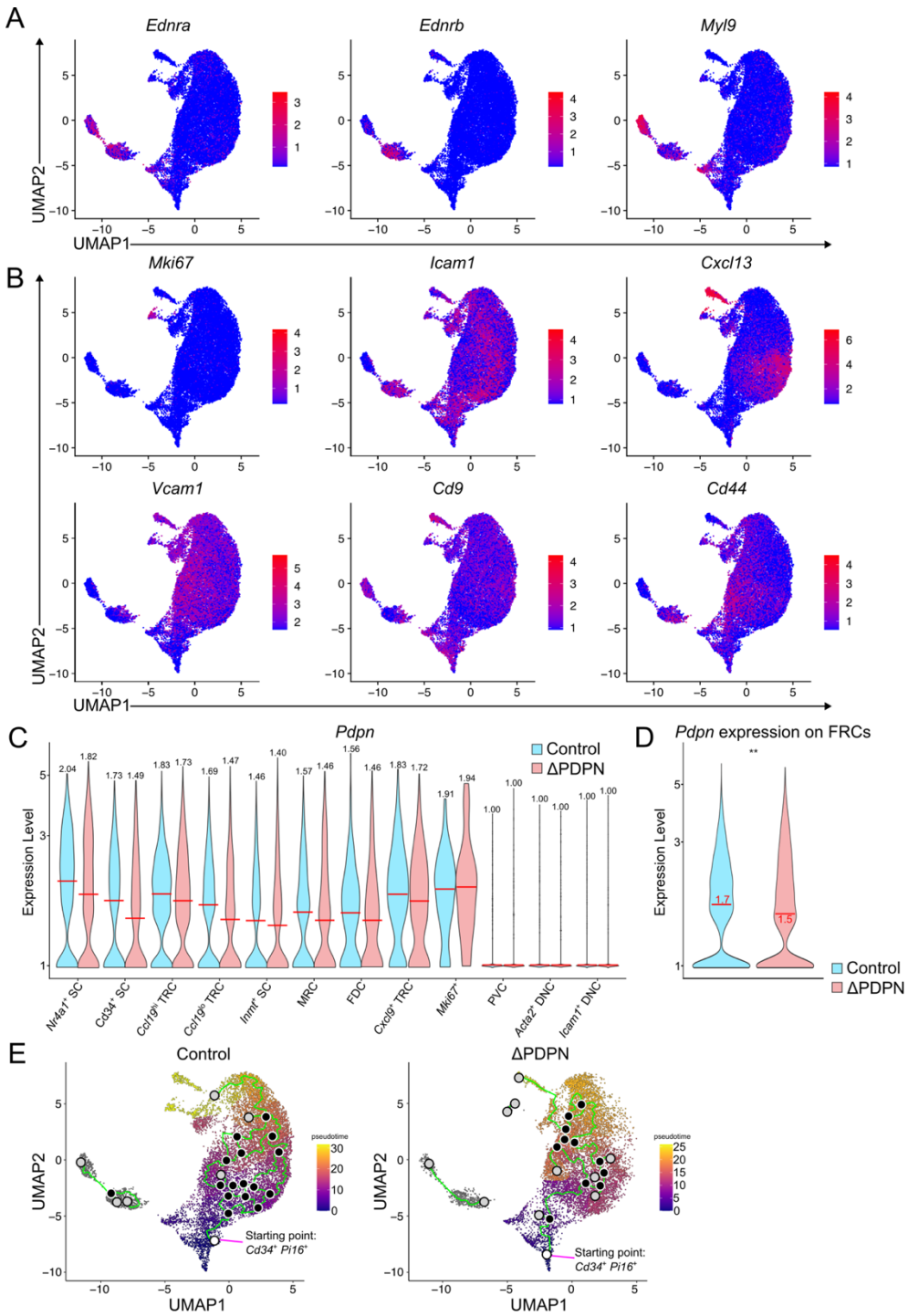

Fig. S2. Fibroblast gene expression and trajectory analysis

(**A**) Expression on fibroblasts UMAPs for genes characterising PDGFRβ⁺ fibroblasts. (**B**) Gene expression on fibroblast UMAPs for markers defining the fibroblasts clusters. (**C**) expression of *Pdpn* across all fibroblast clusters in PDGFRα^{mGFP} (control) or PDGFRα$^{mGFP\Delta PDPN}$ (ΔPDPN) cells and (**D**) on PDGFRα cells. Mann-Whitney test (two tailed), ns = no significance, **p<0.01. (**E**) Trajectory analysis (Monocle3) PDGFRα^{mGFP} (control) or PDGFRα$^{mGFP\Delta PDPN}$ (ΔPDPN) with starting point at *Cd34*⁺*Pi16*⁺ stromal cells (white circle), black circles indicate branch points and light grey circle correspond to a cell fate.

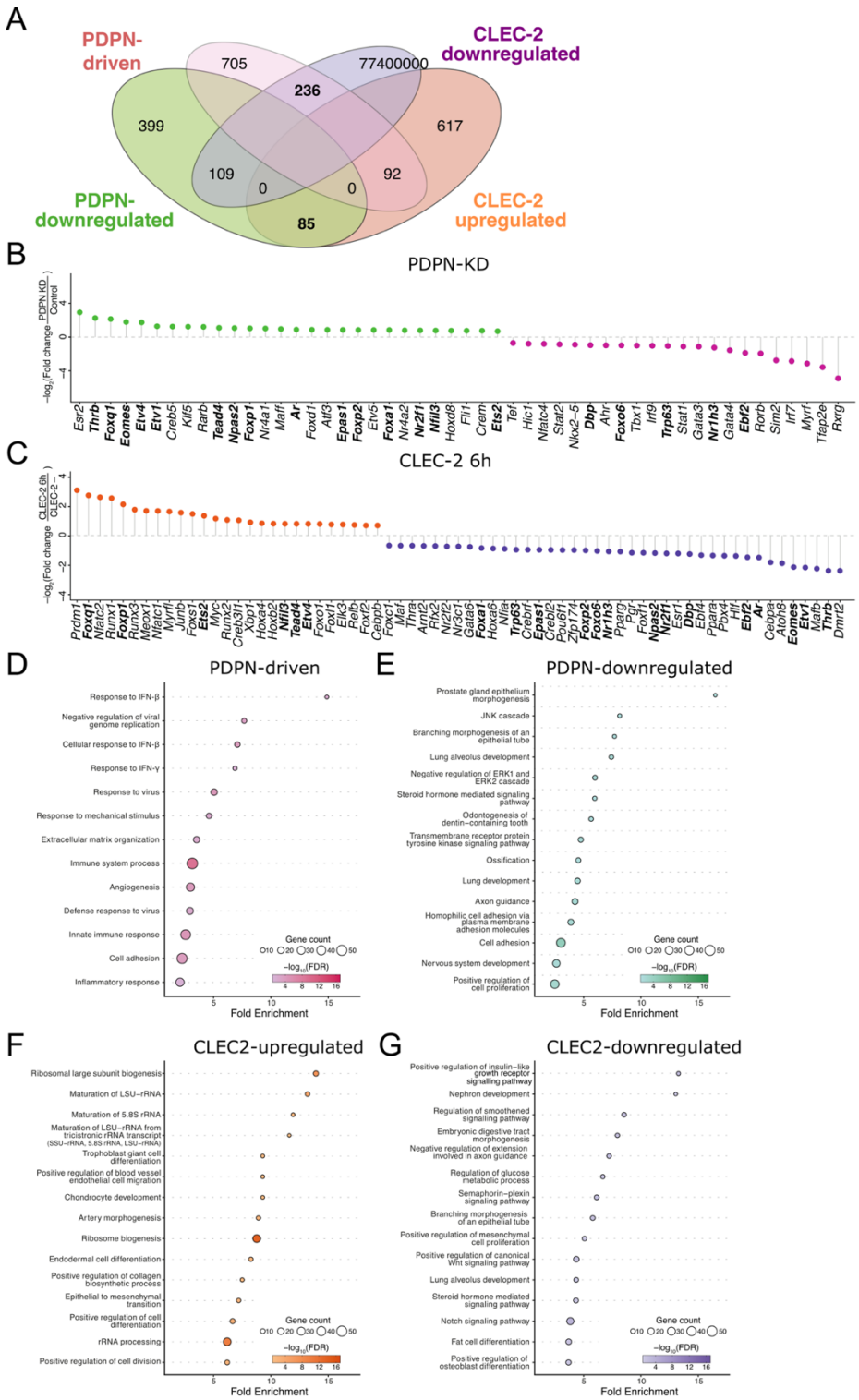

Fig. S3. Functional annotation of the PDPN/CLEC-2 differentially expressed genes

(**A**) Venn diagram of the differentially expressed genes regulated by PDPN-KD or treatment with CLEC-2 after 6h. Transcription factors regulated by (**B**) PDPN-KD or (**C**) CLEC-2 treatment for 6 hours. (**D-G**) Gene enrichment using the GO Term database on DAVID. (**D**) PDPN downregulated (**D**) CLEC-2 upregulated (**F**) and CLEC-2 downregulated (**G**) pathways. Dot colour represents statistical significance ($\log_2$ FDR) and size is proportional to gene count.

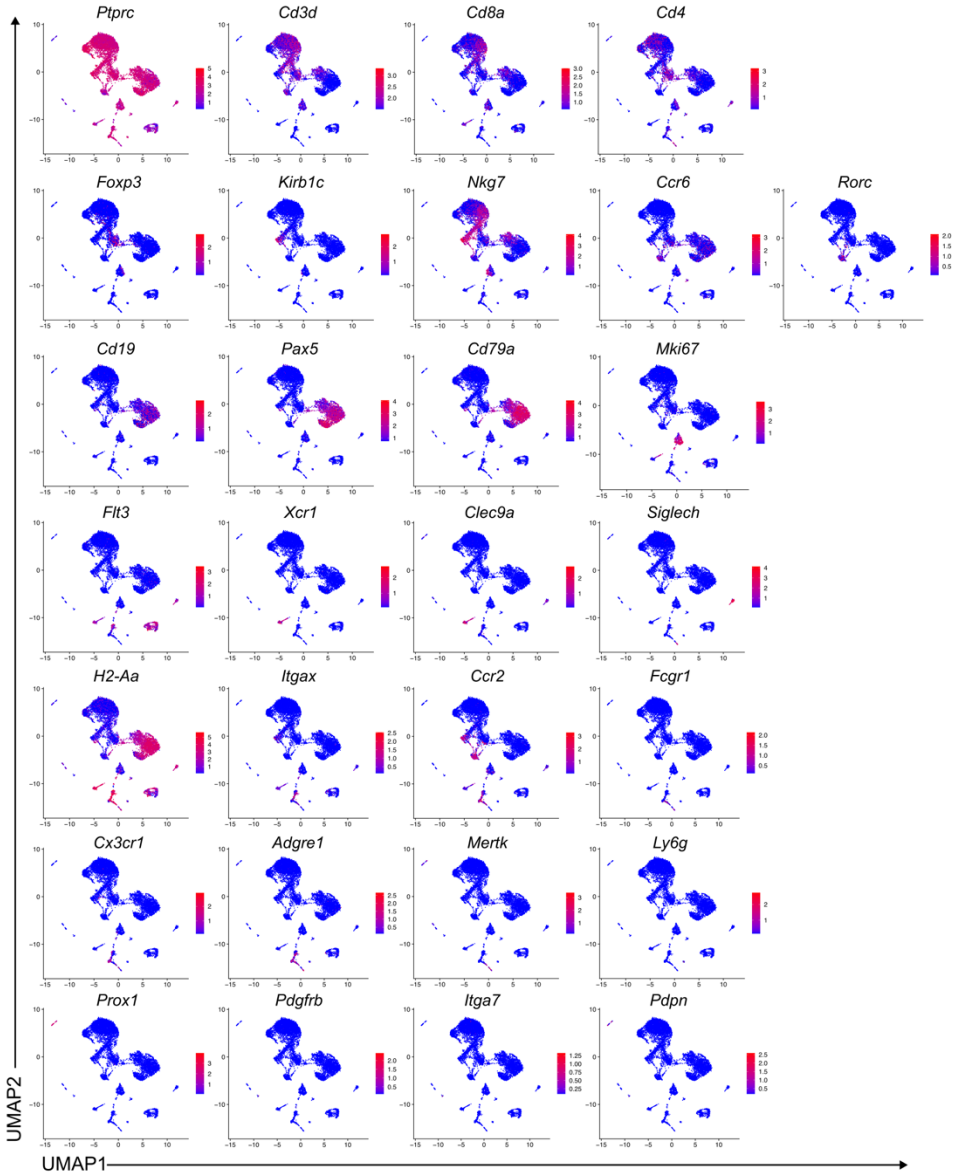

Fig. S4. Expression of genes in CD45⁺ and CD31⁺ enriched cells

UMAP showing key genes used to define CD45⁺CD31⁺ (immune and endothelial cell) clusters.

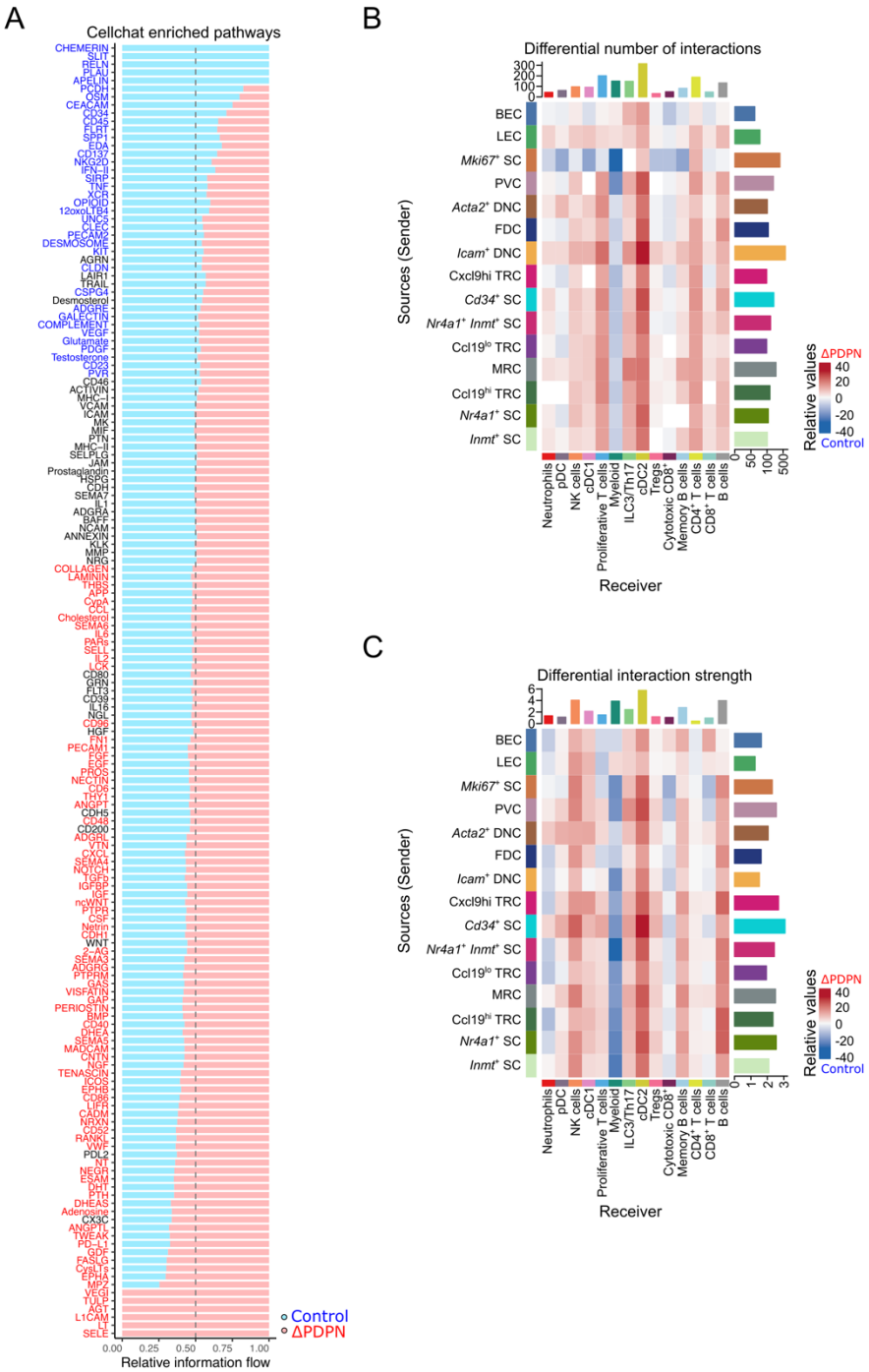

Fig. S5. Cellhat analysis on communication between stromal and immune cells

(**A**) Cellchat enriched pathways between PDGFRα^{mGFP} (Control) or PDGFRα$^{mGFP\Delta PDPN}$ (ΔPDPN) in merged CD45^{-}CD31^{-} and CD45^{+}CD31^{+} datasets. (**B**) Number of interactions and (**C**) interaction strength between stromal and immune cells. CellChat scores between stromal cells (source) and immune cells (receiver) where control is shown in blue and ΔPDPN in red.

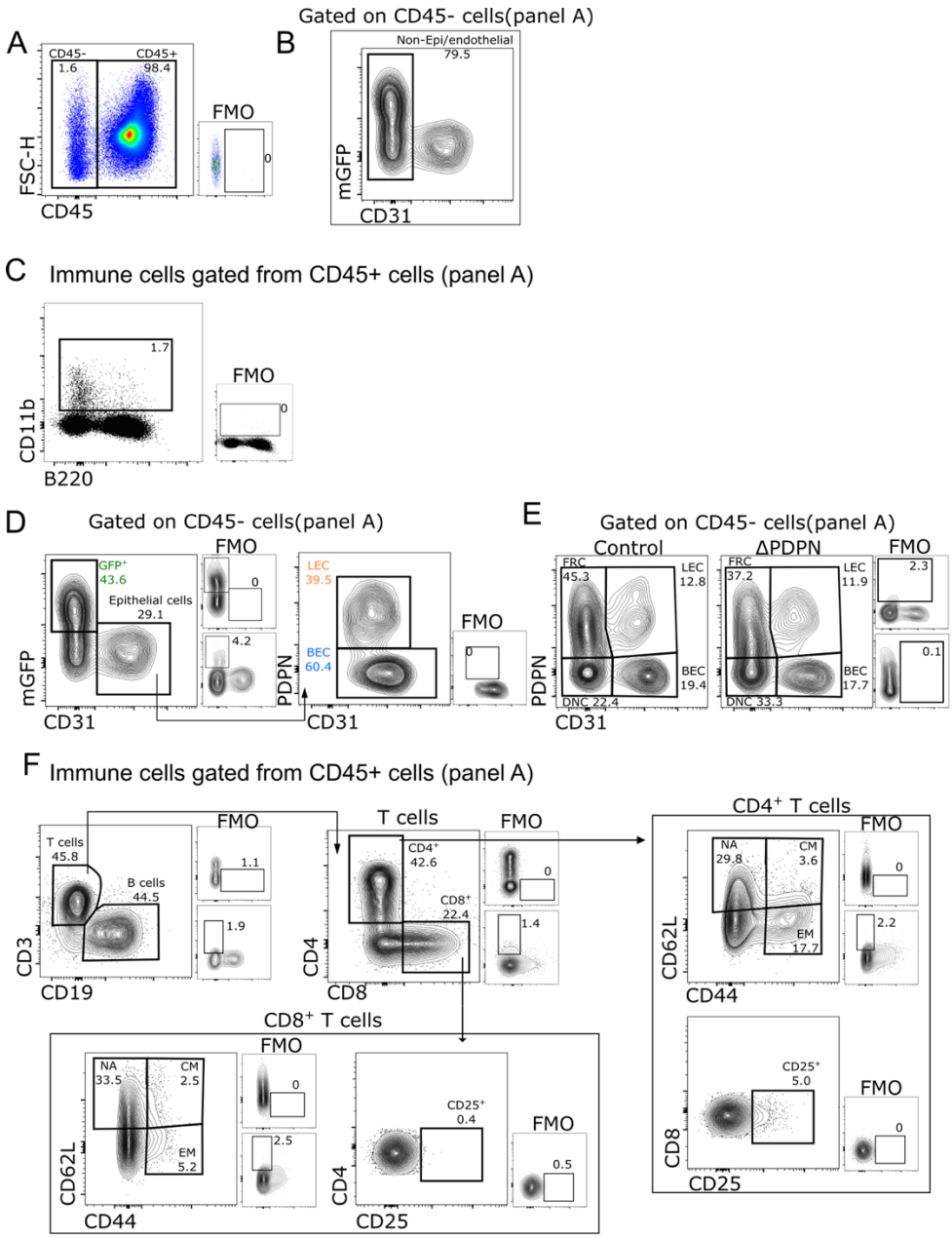

Fig. S6. Gating strategy for stromal and adaptive cells

Flow cytometry gating used to define (**A**) CD45^{-} or CD45^{+} cells. (**B**) Gating of myeloid cells and (**D-E**) gating used to define FRCs, LECs, BECs and DNCs. (**F**) Gating strategy for defining T adaptive cell subsets.

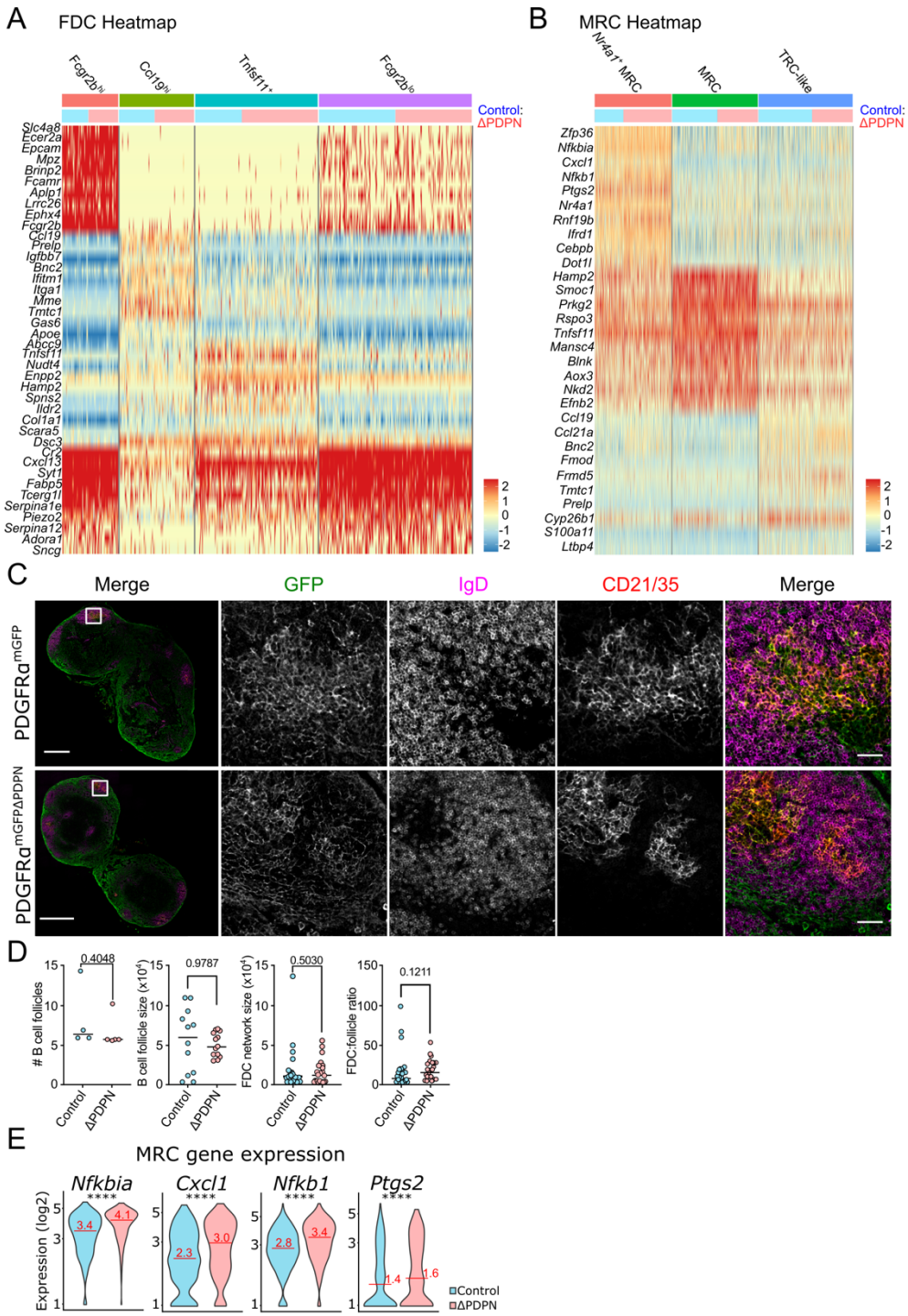

Fig. S7. B cell follicle network organisation and FDC/MRC phenotypes altered in PDGFRα$^{mGFP\Delta PDPN}$ lymph nodes

(**A**) FDC and (**B**) MRC clusters showing Heatmap showing top 10 DEG for each defined subcluster. Ratio of Control (blue) and ΔPDPN (pink) numbers (top row). (**C**) Tilescans of non-immunised PDGFRα^{mGFP} or PDGFRα$^{mGFP\Delta PDPN}$ lymph nodes staining for PDGFRα (GFP), IgD (magenta), CD21/35 (red). (**D**) Analysis of number of B cell follicles, follicle size, FDC network size and FDC to follicle ratio. Mann-Whitney test (two tailed). Scale bar in tilescan is 500 μm and 50 μm in zoomed images. Images representative of 4-5 lymph nodes for each condition from 2 independent experiments. (**E**) Expression of NF-κB pathway genes enriched in MRC cluster. Mann-Whitney test (two tailed), ****p<0.0001.

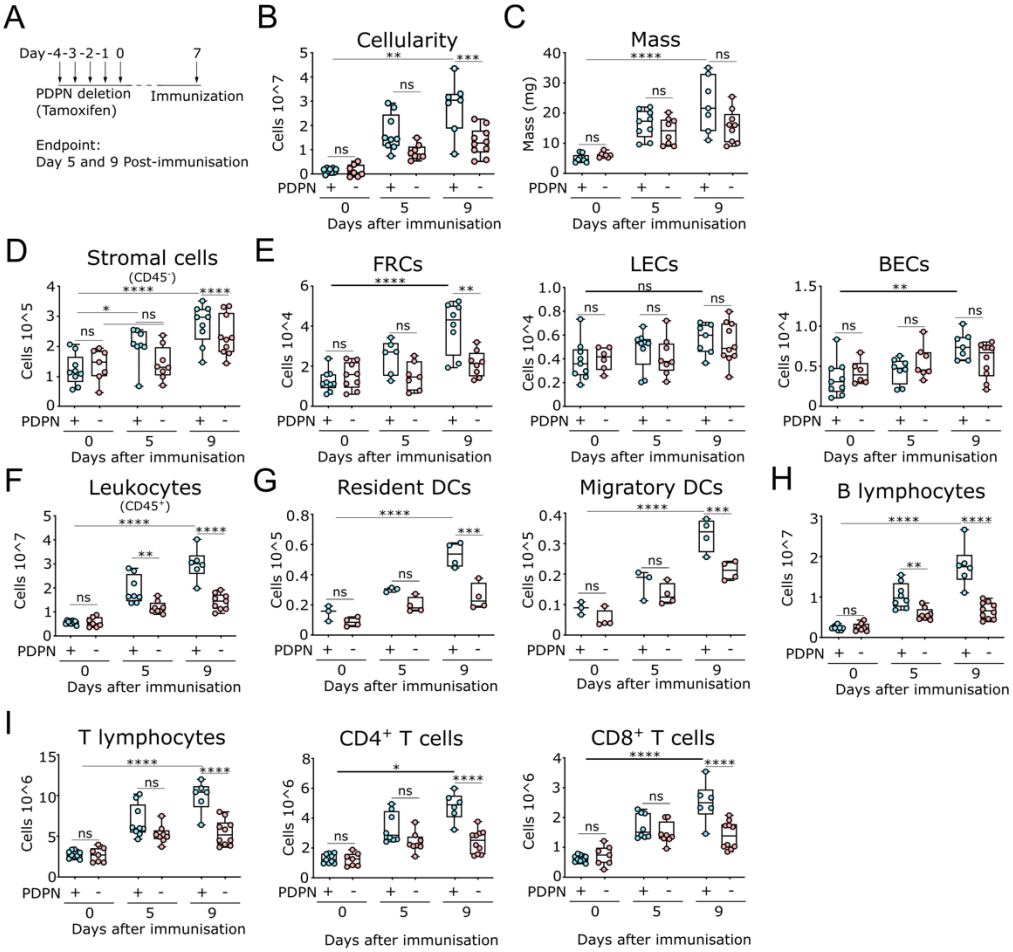

Fig. S8. Lymph node expansion after immunisation is reduced by PDPN deletion.

(**A**) Schematic of experimental design for PDGFRα^{mGFP} (Control) or PDGFR$\alpha^{mGFP\Delta PDPN}$ (ΔPDPN) mice immunisation with Incomplete Freund's Adjuvant with ovalbumin (IFA-OVA). (**B**) Total cellularity and (**C**) lymph node mass measurement. Numbers of (**D**) stromal cells number (**E**) FRCs, LECs, BECs, (**F**) leukocytes, (**G**) Resident DCs, Migratory DCs, (**H**) B lymphocytes, (**I**) T lymphocytes, CD4$^+$ T cells and CD8$^+$ T cells. Flow cytometry gating found on fig. S6. N= 3-5 mice per timepoint representative of 3 independent experiments. Mann-Whitney test (two tailed), ****p<0.0001, ***p<0.001, **p<0.01, *p<0.05, ns=no significance.

56 **Supplementary Tables**

57 Table S1. Gene expression for each fibroblast cluster with condition comparison.

58 Table S2. Differentially expressed gene for each fibroblast cluster.

59 Table S3. Gene expression and proportion between conditions in fibroblast clusters.

60 Table S4. *Nr4a1*$^{+}$ subcluster differentially expressed genes.

61 Table S5. *Ccl19*^{hi} subcluster differentially expressed genes.

62 Table S6. Gene overlap between *in vivo* scRNA-seq and *in vitro* bulk RNA-seq.

63 Table S7. Comparison of gene expression and DESeq *in vitro*.

64 Table S8. STRING analysis *in vitro*.

65 Table S9. Differentially expressed genes in CD45^{+} and CD31^{+} cells.

66 Table S10. Myeloid and macrophage subcluster differentially expressed genes.

67 Table S11. Dendritic cell subcluster differentially expressed genes.

68 Table S12. B cell subcluster differentially expressed genes.

69 Table S13. FDC subcluster differentially expressed genes.

70 Table S14. MRC subcluster differentially expressed genes.

71 Table S15. Materials and consumables.